Published in final edited form as:
Science. 2020 March 13; 367(6483): . doi:10.1126/science.aax9554.

Liquid-liquid phase separation drives skin barrier formation

Felipe Garcia Quiroz[1,*], **Vincent F. Fiore**[1], **John Levorse**[1], **Lisa Polak**[1], **Ellen Wong**[1], **H. Amalia Pasolli**[2], **Elaine Fuchs**[1,†]

[1]Howard Hughes Medical Institute, Robin Chemers Neustein Laboratory of Mammalian Cell Biology and Development, The Rockefeller University, New York, NY 10065, USA.

[2]Electron Microscopy Resource Center, The Rockefeller University, New York, NY 10065, USA.

Abstract

At the body surface, skin's stratified squamous epithelium is challenged by environmental extremes. The surface of the skin is composed of enucleated, flattened surface squames. They derive from underlying, transcriptionally active keratinocytes that display filaggrin-containing keratohyalin granules (KGs) whose function is unclear. Here, we found that filaggrin assembles KGs through liquid-liquid phase separation. The dynamics of phase separation governed terminal differentiation and were disrupted by human skin barrier disease–associated mutations. We used fluorescent sensors to investigate endogenous phase behavior in mice. Phase transitions during epidermal stratification crowded cellular spaces with liquid-like KGs whose coalescence was restricted by keratin filament bundles. We imaged cells as they neared the skin surface and found that environmentally regulated KG phase dynamics drive squame formation. Thus, epidermal structure and function are driven by phase-separation dynamics.

Abstract

INTRODUCTION: Liquid-liquid phase separation of biopolymers has emerged as a driving force for assembling membraneless biomolecular condensates. Despite substantial progress, studying cellular phase separation remains challenging. We became intrigued by enigmatic, membraneless protein granules (keratohyalin granules, KGs) within the terminally differentiating cell layers of mammalian epidermis. As basal progenitors cease to proliferate and begin their upward journey

---

[†] Corresponding author. fuchslb@rockefeller.edu.
[*] Present address: Wallace H. Coulter Department of Biomedical Engineering, Georgia Institute of Technology and Emory University, Atlanta, GA 30322, USA.
Author contributions: F.G.Q. and E.F. conceived the project, designed the experiments, and interpreted the data. F.G.Q. and V.F.F. conceived and performed AFM experiments. J.L. performed lentiviral injections. L.P. established and maintained all relevant mouse lines. E.W. participated in cloning and protein biochemistry. H.A.P. performed and interpreted ultrastructural analyses. F.G.Q. and E.F. wrote the manuscript with contributions from V.F.F.

SUPPLEMENTARY MATERIALS
science.sciencemag.org/content/367/6483/eaax9554/suppl/DC1
Supplementary text

Competing interests: E.F. and F.G.Q. are inventors on a provisional patent application, filed by Rockefeller University, for the use of phase-separation sensors described in this work. The authors declare no other competing interests.

Data and materials availability: All data needed to evaluate the conclusions in the paper are present in the paper and/or the supplementary materials. Plasmids described in the manuscript can be provided by E.F. or F.G.Q. pending a completed material transfer agreement. Requests for these materials should be submitted to fuchslb@rockefeller.edu.

toward the skin surface, they produce differentiation-specific proteins that accumulate within KGs. Upon approaching the surface layers, all cellular organelles and KGs are inexplicably lost, resulting in flattened, dead cellular ghosts (squames) that seal the skin as a tight barrier to the environment.

RATIONALE: In an unbiased proteome-wide in silico search for candidate phase-transition proteins, we previously identified a major KG constituent, filaggrin (FLG), whose truncating mutations are intriguingly linked to human skin barrier disorders. Using advanced tools to study phase-separation behavior in mammalian skin, we pursued the possibility that liquid-liquid phase separation might lie at the root of both epidermal differentiation and human disease.

RESULTS: We found that KGs are liquid-like condensates, which assemble as filaggrin proteins undergo liquid-liquid phase separation in the cytoplasm of epidermal keratinocytes. Disease-associated FLG mutations specifically perturbed or abolished the critical concentration for phase separation–driven assembly of KGs. By developing sensitive, innocuous phase-separation sensors that enable visualization and interrogation of endogenous liquid-liquid phase-separation processes in mice, we found that filaggrin’s phase-separation dynamics crowd the cytoplasm with increasingly viscous KGs that physically affect organelle integrity. Liquid-like coalescence of KGs was restricted by surrounding bundles of differentiation-specific keratin filaments. Probing deeper, we found that as epidermal cells approached the acidic skin surface, phase-transition proteins experienced a rapid, naturally occurring pH shift and dynamically responded, causing the dissipation of their liquid-like KGs to drive squame formation.

CONCLUSION: Through the biophysical lens of liquid-liquid phase separation, our findings shed fresh light on the enigmatic process of skin barrier formation. Our design and deployment of phase-separatz.

Through engineering filaggrins, filaggrin disease–associated variants, and our phase-separation sensors, we unveiled KGs as abundant, liquid-like membraneless organelles. During terminal differentiation, filaggrin family proteins first fuel phase-separation–driven KG assembly and subsequently, KG disassembly. Their liquid-like and pH-sensitive properties ideally equip KGs to sense and respond to the natural environmental gradients that occur at the skin’s surface and to drive the adaptive process of barrier formation.

Liquid-phase condensates have typically been viewed as reaction centers where select components (clients) become enriched for processing or storage within cells. Analogously, KGs may store clients, possibly proteolytic enzymes and nucleases, that are temporally released in a pH-dependent manner to contribute to the self-destructive phase of terminal differentiation. Additionally, however, we provide evidence for biophysical dynamics emerging from condensate assembly, as KGs interspersed by keratin filament bundles massively crowd the keratinocyte cytoplasm and physically distort adjacent organelles. This crowding precedes the ensuing environmental stimuli that trigger disassembly of KGs, enucleation, and possibly other cellular events linked to barrier formation. Overall, the dynamics of liquid-like KGs, actionable by the skin’s varied environmental exposures, expose the epidermis as a tissue driven by phase separation.

Finally, we discovered that filaggrin-truncating mutations and loss of KGs are rooted in maladapted phase-separation dynamics, illuminating why associated skin barrier disorders are

exacerbated by environmental extremes. These insights open the potential for targeting phase behavior to therapeutically treat disorders of the skin's barrier.

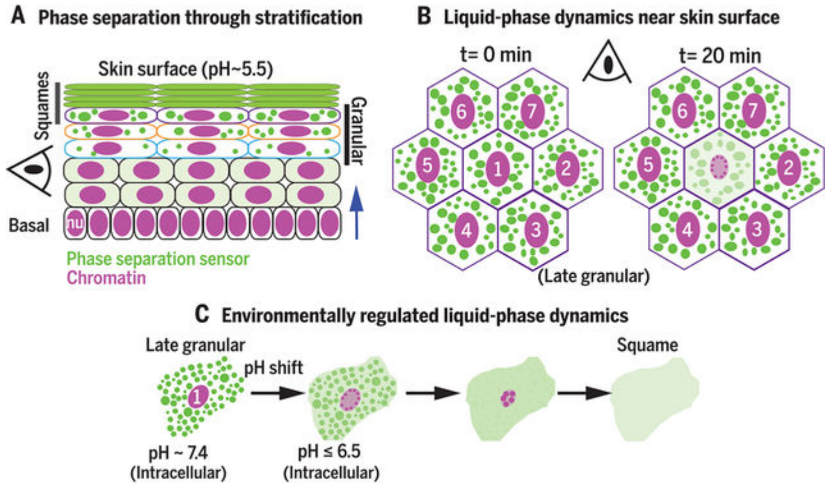

Environmentally regulated liquid-phase dynamics drive skin barrier formation. (A) Using phase-separation sensors, we show that as basal progenitors flux toward the skin surface, they display phase-separation–driven assembly of liquid-like droplets. **(B)** In late-granular cells, these droplets crowd the cytoplasm and dissolve as cells (1) undergo chromatin compaction. **(C)** Near the skin surface, a sudden shift in intracellular pH regulates liquid-phase dynamics to drive squame formation.

Liquid-liquid phase separation of biopolymers has emerged as a major driving force for assembling membraneless bio-molecular condensates (1–3). Such condensates include nucleoli (4), receptor signaling complexes (3, 5), germline granules (1, 6), and stress granules (7). This focus on phase separation has also revealed unexpected insights into a range of biological processes, including genomic organization (8–10), RNA processing (11, 12), mitosis (13, 14), cell adhesion (15), and carbon dioxide fixation in plants (16). However, the study of cellular phase separation remains challenging (17, 18), often relying upon truncated protein mutants, reconstituted systems in nonphysiological buffers, and overexpression or knockin of tagged fusions (17, 19) that can alter a protein's phase-separation behavior.

In mammalian epidermis, a self-renewing inner (basal) layer of progenitors fuels an upward flux of nondividing keratinocytes that stratify to form the skin's surface barrier that excludes pathogens and retains body fluids (Fig. 1A) (20). In early spinous layers, terminally differentiating cells acquire an abundant network of K1- and K10-containing keratin filament bundles. When keratinocytes enter the granular layers, they acquire membraneless protein deposits ("keratohyalin granules," KGs) of enigmatic function (21). As these cells approach the surface layers, global transcription suddenly ceases and both KGs and organelles are lost, giving rise to layers of flattened, dead cellular ghosts (squames) that seal the skin as a tight barrier to the environment.

Our prior proteome-wide in silico search for candidate phase-transition proteins identified a major constituent of KGs, filaggrin (FLG) (22), whose truncating mutations are intriguingly linked to human skin barrier disorders (23) (Fig. 1B and fig. S1). Here, we asked whether liquid-liquid phase separation might lie at the root of both mammalian epidermal differentiation and human disease.

Phase-separation behavior of filaggrin and its paralogs in normal and disease states

Filaggrin and its less-studied (often less-abundant) paralogs are intrinsically disordered repeat proteins with a low-complexity (LC) sequence. Though their sequences are poorly conserved (24) (25, 26), mouse and human filaggrin and their paralogs share similar repeat architecture, LC biases, and localization in the cell within KG-like structures (Fig. 1, B and C; figs. S2 to S4; and table S1).

Like many proteins that drive phase separation, filaggrin family proteins across species exhibit a marked bias for arginine (over similarly charged lysine) to engage in aromatic type interactions (22) (Fig. 1D and fig. S3). They differ in that their only prominent aromatic residue is histidine, rather than tyrosine or phenylalanine (fig. S2). Our prior work showed that histidine-rich, intrinsically disordered proteins (IDPs) must be large to display phase-separation behaviors (22). Notably, both human (~435 to 504 kDa) and mouse filaggrin are among the largest proteins across these proteomes (Fig. 1E). Humans whose filaggrin variants have the greatest repeat numbers exhibit reduced susceptibility to skin inflammation and allergy (23).

To directly examine filaggrin and its disease-associated variants for phase-separation behavior, we first engineered expression vectors driving 1 to 16 human filaggrin repeats (humans have up to 12), each tagged with a fluorescent protein [superfolder green fluorescent protein (sfGFP) or monomeric red fluorescent protein (mRFP)] with or without the non-repeat domains (fig. S5 and table S2). When transfected into immortalized human keratinocytes (HaCATs) under conditions in which filaggrin was not expressed, a single FLG repeat displayed only diffuse cytoplasmic localization (fig. S6A). By contrast, keratinocytes transfected with genes encoding variants of ≥4 repeats efficiently formed KG-like structures. Moreover, proportional to the total repeat numbers, a monotonic increase in density within KG-like granules plateaued beyond the largest known human filaggrins, suggesting that nonphenotypic filaggrins (10 to 12 repeats) optimally define the material properties of KGs (fig. S6B).

Humans with early truncation mutations fail to generate KGs. Such mutations account for >80% of cases among northern Europeans (27). To quantitatively determine how disease-associated mutations alter the critical concentration for phase separation, we incorporated a self-cleavable (p2a) sequence (28) to express equimolar amounts of mRFP-FLG variants and H2B-GFP (as a proxy for variant concentration) (fig. S7A and table S2). Live imaging of transfected HaCATs expressing comparable nuclear GFP revealed a relationship between the number of filaggrin repeats and phase-separation propensity (Fig. 2A). Over a wide range of expression levels, disease-associated mutations with ≤4 repeats exhibited a large increase (~130 to >1500 μM) in critical concentration required for phase separation (Fig. 2B and fig. S7, B to F). By contrast, wild-type filaggrin ($n = 12$) phase separated at ~2 μM. These properties were confirmed by live imaging, exposing the rapid formation and growth of KG-like structures as filaggrin reached its critical concentration for phase separation (Fig. 2C).

Filaggrin and its paralogs belong to the S100-fused type protein family that feature two short “EF hand” calcium-binding motifs (~2% of the protein), N-terminal to the IDP domain. The S100 domain is known to dimerize (29), and when fused to filaggrin variants, it reduced the critical concentration for phase separation (Fig. 2D). Despite these favorable interactions, S100 with mut-n2 FLG mutations still failed to phase separate appreciably even at high concentration (Fig. 2D and fig. S7, B to F). Overall, when compared with mRFP fusions, sfGFP lowered the critical concentrations for phase separation of tagged-FLG variants, although the results were consistent independent of the tag (fig. S7, G and H).

To further explore whether compromised phase separation might underlie disease se verity, we next performed fluorescence recovery after photobleaching (FRAP). As expected for a diffusive process, highly truncated, smaller FLG repeat variants exhibited more rapid recovery than wild-type (WT)–sized proteins (Fig. 3A). However, even the largest FLG variants (>430 KDa) recovered fully within a few seconds (Fig. 3A). The amino and carboxy domains flanking the repeats also affected recovery time. As predicted, the S100 dimerizing domain of FLG variants increased recovery half-life after photobleaching even further, while deletion of the carboxy tail, a small truncation mutation seen in some patients, accelerated recovery (Fig. 3B and fig. S7I). Overall, the dynamic FRAP behavior established filaggrin-containing KGs as biomolecular condensates and distinguished them from mere aggregates in the cell. Moreover, because the S100 domain is cleaved during terminal differentiation, its function is likely to optimize phase separation at earlier stages when filaggrin amounts are low and KGs just begin to form.

Liquid-like behavior of filaggrin granules

Live-cell imaging revealed that HaCATs harboring our engineered filaggrins underwent granule rearrangements and fusion events that are hallmarks of liquid-like droplets (Fig. 3C and movie S1). Individual fusion events were complete within seconds (fig. S8 and movie S2).

To further probe their material properties, we used atomic-force microscopy (AFM). By applying pressure with an AFM probe directly on top of filaggrin granules, they deformed, creating liquid-like streaming around the cell’s nucleus (Fig. 3D, fig. S9, and movie S3). Even unprocessed (more viscous) S100-containing filaggrin granules underwent fusion when pushed into close proximity by the AFM probe (movie S4).

Our photobleaching data suggested that the material properties of KGs may change as a function of filaggrin processing and disease-associated mutations. To test this hypothesis, we performed serial force-indentation measurements across the granule length in HaCATs harboring different filaggrin variants (Fig. 3E and fig. S10). Consistent with a role for the tail domain in tuning the material properties of KGs, AFM revealed a stiffening of the cellular domain spanned by tail-containing granules as compared to filaggrin counterparts that mimicked tail-deficient mutants (Fig. 3F). As suspected from the photobleaching data, unprocessed (S100-containing) filaggrin variants displayed pronounced stiffening (Fig. 3F and fig. S10). Thus, filaggrin granules are mechanically responsive, liquid-like condensates in cells.

Engineering phase separation sensors to interrogate endogenous KGs

Although our tagged filaggrin variants assembled de novo into KG-like structures, it was critical to address whether endogenous KGs in skin assemble through phase separation of filaggrin and if so, how their putative liquid-like properties contributed to epidermal differentiation. To do so, we could not use direct filaggrin tagging to label endogenous KGs, because it altered its biophysical properties (fig. S7G). Similarly, often used client proteins that directly bind to a phase-separating protein scaffold (2, 30, 31) were not suitable, because although they can be recruited to existing liquid-like condensates and be used as carriers of fluorescence, they report scaffold localization irrespective of phase separation. Moreover, with complex differentiation programs in tissues, where processing of the scaffold can occur, the caveats of conventional clients become all the more apparent (fig. S11 and supplementary text).

Thus, we sought to design different clients that would permit probing the phase-separation behavior of endogenous scaffold proteins as their concentration and processing change in living tissues. We aimed for soluble IDP clients that lack phase-separation behavior of their own but copartition efficiently and innocuously into nascent phase-separated condensates by engaging in ultraweak, phase-separation–specific (combinations of charge-charge, cation-pi, pi-pi, hydrogen-bonding, and hydrophobic) interactions with the scaffold (Fig. 4A and fig. S12A).

To engineer such “phase-separation sensors” for endogenous filaggrin, we exploited (i) the nonpathogenic behavior of human filaggrin repeat mutants that possess His:Tyr mutations (fig. S12, B and C) and (ii) the inability of a sole filaggrin repeat to drive phase separation. After documenting the tuned phase-separation characteristics of Tyr-high FLG repeat #8 (r8) variants (r8H1 and r8H2) (22), we then generated variants with related sequence patterns but low sequence identity (ir8H2 and pr8H2). We also engineered proteins smaller than a filaggrin repeat, but with similar compositional biases (eFlg1, ieFlg1, and eFlg2). These proteins displayed a range of phase-separation propensities (Fig. 4B; fig. S12, D to F; table S3; and supplementary text).

For live imaging, our sensors needed a fluorescent tag. Because surface charge of fusion proteins can affect IDP phase-separation behavior (32), we screened Tyr-high sensor variants fused to sfGFPs of varying net charges (33) for those that display high partition coefficients into KGs (figs. S12F and S13, A and B). We selected two +15GFP-based (sfGFP with net charge +15) sensor designs that shared little sequence identity among themselves or the native filaggrin repeat (Fig. 4C). On their own, these sensors showed no phase separation (fig. S13C), but when coexpressed with an mRFP-tagged filaggrin in HaCATs, they partitioned into the de novo assembled KGs (Fig. 4D). In particular, the relocalization of sensor A from the cytoplasm into filaggrin granules (partition coefficient P = 21) compared well to the behavior of filaggrin itself (P = 125) and remained stable over a wide range of sensor A levels (fig. S14A). This enabled faithful reporting of steep concentration gradients across membraneless granule boundaries. Notably, and in contrast to a conventional client that bound stoichiometrically to a filaggrin domain (fig. S14, B to D), FRAP dynamics of mRFP-tagged filaggrin were unaffected by sensor A (Fig. 4E).

Because of FRAP's size dependence, our studies in Fig. 3A were only suggestive that FLG truncating mutations accelerate liquid-like dynamics within KGs. With our designed sensors as internal controls, we could now accurately determine FRAP half-lives and evaluate the liquid-like behavior of KGs formed from different-sized filaggrin mutants. As predicted, KGs assembled from truncated filaggrins differed from their full-length counterparts in displaying sensor recovery dynamics indicative of a decrease in the relative viscosity of KGs (Fig. 4F). Moreover, KGs assembled from tail mutants behaved as less viscous liquids than their tail-containing counterparts. Thus, our phase-separation sensors can integrate into and innocuously report the material properties of liquid-like KGs. Furthermore, our data suggest that patient disease phenotypes are indeed linked to shifts in the liquid-like behavior of mutant KGs.

Crowding of liquid-like KGs within skin cells in tissue

Our ultimate goal was to interrogate the dynamics of these liquid-liquid phase transitions in vivo in the skin epidermis. To this end, we used a noninvasive in utero lentiviral delivery system to selectively, efficiently, and stably transduce the single layer of embryonic day 9.5 (E9.5) mouse skin epithelium with doxycyclineinducible transgenes encoding our sensors (fig. S15). To induce expression during epidermal differentiation, we transduced embryos carrying a doxycycline-sensitive reverse tetracyclinetransactivator (rtTA) driven by the human *Involucrin* (*Ivl*) promoter (34).

Once the skin barrier was fully mature (E18.5), doxycycline-fed embryos were subjected to live imaging and/or immunofluorescence microscopy. Sagittal confocal views revealed that bright sensor signal was confined to filaggrin-expressing granular layers, while planar views showed a robust array of sensor-labeled KGs in these cells (Fig. 5A). Moreover, and in marked contrast to conventional antibodies against filaggrin (35), the sensors penetrated even the large granules of the most mature (late) granular layer (fig. S16).

The marked level of KG crowding seemed incompatible with liquid-like behavior. To gain further insights, we performed live imaging and monitored keratinocyte flux through the granular layers of skin (36). Early granular cells displayed only a few KGs, whose numbers appeared to increase through de novo granule formation (Fig. 5B). Over a half day of imaging, occasional fusions that resolved within minutes into a round granule pointed to liquid-like behavior (fig. S17 and movie S5). Moreover, for both sensor A or B, signal recovery was rapid after photobleaching KGs within the mid-granular layer, further underscoring the liquid-like behavior of these endogenous KGs (Fig. 5, C and D).

Despite these liquid-like features, most existing KGs grew robustly without undergoing fusion (Fig. 5E and movie S6). Even KGs within the earliest granular layers in skin tissue exhibited liquid-like properties distinct from those of KG-like condensates that formed in

HaCATs when transfected to express tagged filaggrin (Fig. 5F). Moreover, when the sensor's nuclear export signal was removed and sensor FRAP half-life was measured within nucleoli, only filaggrin-containing KGs in tissue appeared to be relatively more viscous than the nucleolus in keratinocytes.

Probing deeper, we noticed that granular cells exhibited substantial morphological changes as they transited through the granular layers and became increasingly crowded with KGs (Fig. 5G). Correspondingly, photobleaching these KGs within early, middle, and late granular cells revealed a gradual reduction in sensor dynamics as cells moved toward the skin surface. This increase in relative viscosity of skin KGs was also seen in stratifying cultures of primary human epidermal keratinocytes, which, unlike immortalized keratinocytes, formed endogenous KGs that were of similar size and displayed liquid-like dynamics similar to those of KGs in the early- and midgranular layers of mouse epidermis (Fig. 5H). Thus, despite pronounced species-specific divergence in filaggrin sequence, the preservation of KG's finely tuned liquid-like behavior pointed to an underlying physiological relevance.

Stabilization of liquid-like membraneless organelles

Although the rarity of fusion events among densely packed KGs might simply reflect their apparent viscosity, it was also possible that additional facets of terminal differentiation might be contributing to this puzzling behavior. Notably, the granular layer also displays an abundant network of terminal differentiation- specific keratins 1 and 10 (K1/K10) filaments. This prompted us to test whether keratin filaments might impede KGs from fusing and allow them to crowd the cytoplasm as stable organelles. When HaCATs were transduced with doxycycline-inducible human mRFP-K10 (table S4), hK10 incorporated into the endogenous network of basal K5/K14 filaments (37). Upon cotransfection with sfGFP-FLG to drive KG formation, many of the mRFP-tagged keratin bundles encased KGs (Fig. 6A). Live imaging showed that these KGs spent prolonged periods of seemingly inert activity. However, in regions where these KGs dislodged from filaments and became uncaged, KGs were mobile and frequently fused with other sfGFP-tagged KGs (Fig. 6B, fig. S18A, and movie S7). This may explain previous perplexing observations that unusually large KGs are produced after genetic ablation of *Krt*10 in mouse skin (38).

Keratins possess a central coiled-coil "rod" domain that initiates heterodimer formation and forms the backbone of the 10-nm intermediate filament (39). Whereas K5/K14 keratins of proliferative progenitors have short amino-and carboxy-LC domains, the large LC domains of K1/K10 keratins (40) are thought to protrude along the outer surface of the filament and bundle into cable-like filaments.

Intrigued by the packing of K10-containing filaments around filaggrin granules, we next asked whether their distinctive features might facilitate interactions with KGs. Examining the behaviors of mCherry fused to one, both, or neither of the hK10 LC domains (table S4), we found that each was diffuse in the cytoplasm of cultured keratinocytes in the absence of KGs (Fig. 6C and fig. S18). By contrast, when sfGFP-tagged filaggrin and its KGs were present, mCherry was excluded from KGs, while both mCherry constructs with hK10 LC domains partially partitioned into KGs. Moreover, the critical concentration for phase separation of sfGFP-tagged filaggrin was reduced in the presence of the K10 keratin network without altering FLG density within KGs (Fig. 6, D and E). Thus, weak interactions between KGs and the LC domains of terminal differentiation–associated keratins may promote the caging and stabilization of KGs in skin.

To further explore this possibility, we transduced both our phase-separation sensor and suprabasal-inducible mRFP-hK10 constructs into E9.5 embryos and performed live imaging on E18.5 skin explants. Whereas early granular cells displayed small, relatively sparse KGs surrounded by a well-defined network of K10-containing filaments, mid-granular cells exhibited a denser keratin network interwoven among larger, more abundant KGs that remained caged and hence unable to fuse (Fig. 6, F and G). Our findings suggest a model whereby reciprocal density-dependent interactions between LC domains of terminal differentiation–specific keratins and KGs structure the cytoplasm to form an elaborate, interwoven network of stabilized liquid-like KGs and keratin filament bundles.

Liquid phase KG dynamics, enucleation, and environmental sensitivity

We posited that progressive crowding by keratin-stabilized KGs might distort the nucleus and other organelles in a fashion that could contribute to their destruction at the critical granular–to–stratum corneum transition. If so, this could explain why nuclei are often aberrantly retained in the outer skin layers of patients who also lack KGs (41).

Consistent with this notion, KGs assembled de novo in HaCATs from WT repeat filaggrins prominently deformed nuclei, whereas KGs assembled from disease-associated FLG mutants instead wetted the nuclear surface without deformation (Fig. 7A and fig. S19, A and B). Endogenous KGs in primary human keratinocytes also induced prominent nuclear deformation (fig. S19C). Similarly, when we transduced embryos with H2B-RFP and our sensors and monitored the maturation of granular cells by live imaging, we found that mature granular cell nuclei were markedly deformed as KG density increased in skin (Fig. 7B and fig. S19D).

As granular cells move upward to complete their final stage of differentiation, they enucleate and lose their KGs to form flattened squames (Fig. 1A). These events were difficult to capture by live imaging, because the process was very rapid, occurring over 2 hours (fig. S20). However, when we captured enucleation events, they were always preceded by chromatin compaction and then chromatin loss and nuclear destruction (Fig. 7C and movie S8). Moreover, just as chromatin began to show signs of compaction, KGs began to dissolve, as revealed by a progressive shift in the phase sensor’s localization from a granular-like state to being diffuse in the cytoplasm (Fig. 7C and fig. S21). This rapid shift indicated a marked change in the liquid-like properties of KGs and suggested that these terminal events may also be rooted in liquid-phase dynamics.

Probing further, we found that Flg knockdown in skin not only depleted KGs but also delayed the nuclear degradation process (Fig. 7D). This was accompanied by increased transepidermal water loss (TEWL) through the skin barrier. Thus, KGs accelerate loss of membrane-bound organelles, an essential feature of skin barrier formation.

Given the inherent environmental responsiveness of intrinsically disordered proteins (42, 43), we wondered whether the marked shift in KG dynamics late in terminal differentiation might be fueled by the environmental changes that naturally occur near or at the skin surface. In particular, whereas prolifer ative basal progenitors experience physiological pH (7.4), the skin surface is acidic (pH ~5.5) (44). Because filaggrin is rich in histidine, whose physiological acid dissociation constant (pK_a) is ~6.1 (45), we posited that this natural difference in extracellular pH may also reflect intracellularly and in part be triggering the KG changes that we had detected at the granular- to–stratum corneum transition.

To detect intracellular pH shifts, we first transduced HaCATs with either mNectarine or SEpHlourin reporters, which rapidly lose fluorescence upon shifting from pH 7.4 to pH 6.3 (fig. S22). When the extracellular pH was decreased to elicit an intracellular pH shift from 7.4 to ~6.2 to 6.5, de novo–assembled KGs in HaCATs changed profoundly. In live imaging, both filaggrin and the sensor (which by design, is also rich in histidine) displayed increased cytoplasmic and diminished KG-like localization concomitant with this intra-cellular pH shift (Fig. 7E and fig. S23). Similar changes were seen in endogenous KGs of differentiated primary human epidermal keratinocytes when they experienced this pH shift (fig. S24A).

Given the pH sensitivity of KGs, we then turned to investigating this process in vivo. We introduced our pH reporters into mice along with either our phase-separation sensor or H2BRFP and through live imaging, monitored the natural intracellular pH shifts that we surmised would occur as granular cells approached the acidic skin surface. Over time, as each granular cell progressed to the critical granular-to-corneum transition, it experienced a sudden shift in pH, as detected by our intracellular reporters (Fig. 7F). This rapid endogenous pH shift invariably coincided with the initiation of KG dissolution (top panels) and coincided with or immediately preceded an increase in chromatin compaction (bottom panels). Moreover, within 2 hours of KG dissolution and nuclear compaction, imaged granular cells within the epidermis had undergone morphological changes characteristic of enucleation and squame formation (fig. S24B and movie S6).

Finally, we took skin explants from embryos transduced with phase sensor, H2BRFP, and either scrambled or filaggrin short hairpin RNAs (shRNAs) and performed live imaging immediately after shifting the extracellular pH in the medium. When the natural intracellular pH transition was accelerated, granular cell KGs showed signs of disassembly, and chromatin compaction became pronounced (Fig. 7G, top panels). This pH shift did not trigger chromatin compaction in skin devoid of KGs (bottom panels). Thus, the pH shift appears to function specifically in altering the material properties of histidine-rich KGs, which in turn promote chromatin compaction, enucleation, and skin barrier establishment. Furthermore, enucleation events in skin are likely driven by a combination of nuclear deformation and pH-driven release of as yet undetermined KG components.

Discussion

Our design and deployment of a class of innocuous client protein provides a general strategy to analyze endogenous liquid-liquid phase separation dynamics across biological systems in a nondisruptive manner. We envision that these in vivo phase-separation sensors may be further functionalized to incorporate enzymes evolved for proximity proteomics (46, 47), potentially enabling—without perturbing endogenous scaffold proteins—the molecular and biophysical interrogation of endogenous liquid-liquid phase separation in organoids, tissues, and living organisms.

We used this strategy to illuminate, through the lens of phase separation, the process of skin barrier formation, which entails the appearance of hitherto enigmatic KGs in the granular layer and then their sudden disappearance as epidermal cells undergo a poorly understood transition to the stratum corneum. These granules, long puzzling to skin biologists (48), had been viewed as inert, cytoplasmic aggregates of filaggrin, which eventually became cleaved into smaller fragments and amino acid derivatives to promote keratin filament bundling (21) and stratum corneum hydration (24). Despite decades of research and mutations linked to atopic dermatitis (23), no clear function had been established for KGs, filaggrin, or filaggrin paralogs that also accumulate as granular deposits in epithelial tissues (49, 50).

Through the engineering of filaggrins and filaggrin disease-associated variants and also phase-separation sensors, we have now shown that KGs are abundant, liquid-like membraneless organelles, which, through their phase-separation–driven assembly and then disassembly, function to structure the cytoplasm and drive an environmentally sensitive program of terminal differentiation in the epidermis. By virtue of their mechanical and pH-sensitive properties, KGs are ideally equipped to confer environmental responsiveness to the rapid and adaptive process of skin barrier formation. The discovery that filaggrin-truncating mutations and loss of KGs are rooted in altered phase-separation dynamics begins to shed light on why associated skin barrier disorders are exacerbated by environmental extremes. These insights open the potential for targeting phase behavior to therapeutically treat disorders of the skin's barrier.

Liquid-phase condensates have typically been viewed as reaction centers where select components (clients) become enriched for processing or storage within cells (2). Analogously, KGs may store clients, possibly proteolytic enzymes and nucleases, that are timely (in a pH-dependent fashion) and rapidly released to promote the self-destructive phase of forming the skin barrier. Additionally, squame formation likely exploits general biophysical consequences of KG assembly, because KGs interspersed by keratin filament bundles massively crowd the keratinocyte cytoplasm and physically distort adjacent organelles prior to the ensuing environmental stimuli that trigger KG disassembly. Overall, the environmentally sensitive dynamics of liquid-like KGs, actionable by the skin's varied environmental exposures, expose the epidermis as a tissue driven by phase separation.

Materials and methods

Sequence analysis of filaggrin and its paralogs

Proteomes were downloaded as FASTA files from UniProt (https://www.uniprot.org/). For the analysis of protein domains known to drive liquid-liquid phase separation (fig. S3), we downloaded the complete set (>100) of proteins from the PhaSEPro database (51). We implemented a script (available upon request) in MATLAB R2016a to extract protein size, amino acid abundance, and Arg-bias of all annotated proteins. Arg-bias was calculated as the total number of arginine residues relative to the total number of positively charged residues (R+K). To calculate relevant sequence parameters (length, amino acid composition, hydropathy, Arg-bias) in FLG and its paralogs across species, we implemented a script (available upon request) in MATLAB R2016a. Hydropathy was calculated as the average level across all residues in a protein, using Kyte-Doolittle's scale (52). Except for human Flg (and its paralogs), most mammalian Flg and Flg paralogs in mammals remain poorly annotated or poorly sequenced in publically available genome and protein databases. Table S1 shows the sequences that we used as input material and details of their manual curation. To characterize nonsynonymous mutations in human filaggrin, we downloaded known single-nucleotide polymorphism (SNPs) in the human Flg gene (not annotated in ClinVar) from NIH's dbSNP database (https://www.ncbi.nlm.nih.gov/snp/) and from the GnomAD browser (https://gnomad.broadinstitute.org/gene/ENSG00000143631). We used custom-made MATLAB scripts (included in the supplementary text) to filter for unique SNPs corresponding to nonsynonymous mutations. This script also calculated the overall percentage of mutations assigned to each of the 20 naturally occurring amino acid residues. By generating 1000 unique Flg mutant genes through random single-nucleotide mutations in Flg cDNA (script available upon request), we also estimated the expected random mutational burden per residue. From the total SNPs, we identified 405 SNPs involving mutations of His codons. The script then identified the mutational landscape involving these SNPs and their corresponding nonsynonymous codons (encoding Asp, Leu, Asn, Pro, Gln, Arg, and Tyr).

Synthesis of repetitive DNAs encoding filaggrin and filaggrin variants

To assemble repetitive DNAs, we used recursive directional ligation by plasmid-reconstruction (PRe-RDL) (53), with minor modifications. Specifically, we used a modified pET-24a(+) vector as published (53), but eliminated the terminal Tyr-stop-stop sequence to avoid altering the hydropathy of FLG sequences. Instead, the modified vector uses a terminal Gly-stop-stop-stop sequence. Synthetic gblocks were from IDT (Integrated DNA Technologies) and encoded the eight repeat in human FLG (repeat #8, here referred as r8), sfGFP, mRFP1, and the S100 domain of human FLG. We chose r8 as this repeat is often duplicated in humans, yielding FLG variants with 11 (this is the most common of all human FLG variants) or 12 repeats. The specific choice of a repeat (among human FLG repeats 1 to 10), however, is otherwise trivial, as individual FLG repeats are nearly identical in sequence (with >90% sequence identity in humans and typically >99% in mice). We performed iterative rounds of PRe-RDL with the r8 gblock to build genes with up to 16 concatemers of r8. These genes were then modified to generate variants with the C-terminal tail domain of human FLG (table S2). DNA sequences were verified by Sanger sequencing (Genewiz, NJ) whenever possible. For long repetitive DNAs beyond the reach of Sanger sequencing, to confirm proper concatamerization of sequence-verified domains, we relied on gene size (judged by conventional DNA gel electrophoresis) and subsequent validation of expected protein properties (size and diffusion properties) upon expression in *Escherichia coli* or mammalian cells. For mammalian expression, we subcloned fully-assembled repeat genes into a modified pMAX vector (Amaxa). See table S2 for protein sequences for all constructs. To build genes with nuclear reporters of FLG concentration in the cell, we further modified our pMAX-based genes encoding FLG repeats to replace the N-terminal fluorescent protein with genes fragments encoding H2BGFP-(p2a)-mRFP, H2BRFP-(p2a)-sfGFP or H2BGFP-(p2a)-S100-mRFP (see table S2 for sequence details). (p2a) is a codon-optimized DNA sequence that self-cleaves during translation and so enables the synthesis of two proteins from a single transcript (28). We also built pMAX vectors encoding H2BRFP-(p2a)-H2BGFP and H2BGFP-(p2a)-H2BRFP to validate the equimolar synthesis of individual (p2a)-linked proteins.

Synthesis of phase-separation sensors

Table S3 includes the sequence information for all sensor domains reported in Fig. 4B. The rationale for the generation of these proteins is explained in detail in the supplementary text. Corresponding genes were synthesized by IDT as gblocks and cloned into modified pMAX vectors as described above for genes encoding FLG variants. We purchased additional gblocks encoding previously published supercharged variants of sfGFP: +15GFP and −20GFP. All constructs, unless indicated, include an optimized short nuclear export signal (54) (LELLEDLTL) as linker between the N-terminal fluorescent proteins and the sensor domain. To test the intrinsic phase separation propensity of individual sensor domains, we artificially enhanced their phase-separation capacity by synthesizing variants with a C-terminal trimerization domain. We generated constructs with one of two trimerization domains: NC1 domain from human COL18A1 (P39060, Isoform 1, residues1442–1496) (55) or a fibritin fragment from bacteriophage T4 (so-called foldon domain) (56).

Synthesis of genes encoding human K10 and its low-complexity domains

We used polymerase chain reaction (PCR) to amplify a fragment of the Krt10 gene spanning the N-terminal LC domain and the complete central coiled-coil rod domain (forward primer: TAATCATCGATCGGATGGCTCTGTTCGATACAGCTCAAGCAAGCACTACTCTT; reverse primer:TAAGCAGGGGATCCCTCTCCTTCTAGCAGGCTGCGGTAGGTTTG) using KRT10 cDNA (NM_000421.2; from Origene). These primers added restriction sites for Pvu I and Bam HI at the N and C terminus, respectively, for seamless restriction into a pMAX vector harboring an N-terminal mRFP sequence and the C-terminal LC domain. The C-terminal LC domain was synthesized by IDT as a gblock. Similarly, we also obtained a gblock encoding the N-terminal LC domain flanked by Nhe I and Xma I sites, which we inserted into our modified pMAX vector for building a gene encoding a fusion to mCherry. This vector was further modified between Bam HI and Eco RI sites to introduce the C-terminal LC domain and generate mCherry fusions harboring both K10 LC domains. These constructs are listed in table S4. Because of Origene’s third-party restrictions, we regret that we are unable to distribute our full-length mRFP-K10 construct, which contain material from Origene SC122561. However, mRFP-K10 may be reconstructed by following the protocol above and obtaining one of our LC constructs as well as Origene SC122561.

Characterization of filaggrin-like proteins and phase-separation sensors

To drive efficient expression of the relevant repetitive proteins, we transfected the corresponding pMAX plasmids into HaCATs (57). We routinely expanded HaCATs in low-calcium (50 μM) epidermal cell culture media (58) and then transfected them in glass-bottom 24-well plates containing CnT-PR media (CELLnTEC, Switzerland). Following the instructions of the manufacturer, we typically used lipofectamine 3000 (Invitrogen) to transfect cells with 0.5 to 3.5 mg of each plasmid. One day after transfection, we changed media to a prodifferentiation media, CnT-PR-D (CELLnTEC, Switzerland) supplemented with 1.5 mM $CaCl_2$ and proceeded to use a spinning-disk confocal microscope to image cells 6 to 9 hours later. Live imaging was conducted with cells at 37°C and under a controlled CO_2 environment. To calculate the phase-separation propensity of FLG repeat proteins, we operationally defined it as the percentage of total (background-corrected) fluorescent signal residing within phase-separated granules and based on maximum intensity projections of live imaging data using ImageJ. Concentration values for FLG variants were determined from the nuclear H2B reporter signal (adjusted by total cell area) in each cell to sensitively measure protein concentration even at low expression levels when FLG proteins are diffuse. Whenever we observed a concentration-dependent increase in phase separation propensity, we applied a logistic fit [$y = (-100/(1 + (x/x0)\text{\^{}}P)) + 100$, as expected for a phase transition] using OriginPro software (OriginLab). Using these fits, we approximated the critical concentration for phase separation as the half-maximal effective concentration (EC$_{50}$) of the logistic fit. The EC$_{50}$ represents the concentration at which most cells reach a phase-separation propensity of 50% —wherein the total number of molecules in the dilute phase equals the number of molecules in the high-concentration density phase. Although phase separation happens with a given (low) probability below the EC$_{50}$, the concentration fluctuations that potently drive phase separation near the true critical concentration of the system become dominant near the EC$_{50}$, which justifies its definition as an experimental approximation to the critical value. To study protein dynamics within granules, we photobleached circular regions (0.54 mm in diameter) of interest at the center of granules and imaged the process of recovery at 200-ms intervals. For data analysis, we normalized the background-corrected fluorescence within the region of interest to the background-corrected average granule fluorescence prior to photobleaching and then corrected for loss of fluorescence in the granule area outside of the region of interest throughout the imaging process. To calculate recovery half-lives, we fitted the post-bleaching normalized data using OriginPro and a standard exponential growth curve: $f = A(1 - \hat{e}(-xt))$. Half-lives (time when $f = 0.5$) were estimated as $\mathrm{Ln}(0.5)/(-t)$. The approach to studying the behavior of phase-separation sensors is similar to the approach described for FLG variants. In addition to vectors harboring tagged-FLG proteins, the transfection mixture included a second pMAX vector encoding sensor variants (table S3). For photobleaching measurements, we first obtained photobleaching data for the mRFP1-tagged FLG protein, followed by photobleaching data for (+15GFP-tagged) sensor A in the same granule. Sensor data were processed and analyzed as for tagged-FLG proteins.

Atomic force microscopy (AFM) measurements

To enable access of the AFM probe to filaggrin granules within cells, we transfected HaCATs in 50-mm glass-bottom dishes (Fluorodish, FD5040, World Provision Instruments). The transfection mixture consisted of two pMAX vectors: one vector harbored a H2B-RFP gene and was common to all transfection reactions, whereas the second vector encoded one of the indicated FLG variants [sfGFP-(r8)8, sfGFP-(r8)8-Tail or S100-sfGFP-(r8)8-Tail; see table S2]. One day after transfection, we added pro-differentiation media (CnT-PR-D) supplemented to 1.5 mM $CaCl_2$. Cells were transported (at 37°C) soon after or up to 24 hours later to the Molecular Cytology core facility of Memorial Sloan Kettering Cancer Center (MSKCC) for AFM measurements using a microscope stage at 37°C. AFM force measurements and manual deformations of sfGFP-tagged FLG granules were performed using an MFP-3D AFM (Asylum Research) combined with an Axio Scope inverted optical microscope (Zeiss). We used silicon nitride probes with a 5-mm-diameter spherical tip (Novascan). Cantilever spring constants were measured before sample analysis using the thermal fluctuation method, with nominal values of ~100 pN/nm. 5 μm by 5 μm force maps were acquired with 10 force points per axial dimension (0.5 mm spacing) atop sfGFP-tagged FLG granules identified using the bright-field and GFP optical images. Measurements were made using a cantilever deflection set point of 10 nN and scan rate of 1 Hz. Bright-field (AFM probe), GFP (FLG variant), and H2B-RFP (nuclei) images were acquired for each cell and granule measured to enable force map and optical image co-registration. Live-video bright-field images were also taken during force map acquisition to observe granule and cellular deformations. Force-indentation curves were analyzed using a modified Hertz model for the contact mechanics of spherical elastic bodies. The sample Poisson’s ratio was 0.33, and a power law of 1.5 was used to model tip geometry. To observe granule displacement and flow following force application, the AFM tip was manually placed adjacent to sfGFP-tagged FLG granules using a micrometer. During live video-rate (14 frames/s) image acquisition (bright-field and GFP), force was manually applied with the AFM probe in the absence of force set point feedback via micrometer manipulation.

Mice and lentiviral transduction

Mice were housed and cared for in an AAALAC-accredited facility, and all animal experiments were conducted in accordance with IACUC-approved protocols. We obtained hIVL-rtTA FVB mouse embryos from J. Segre at the National Institutes of Health (NIH). For rapid generation of mice with genetically modified skin, we used noninvasive, ultrasound-guided in utero lentiviral-mediated delivery of pLKO.1-based expression constructs and shRNAs (Sigma-Aldrich), which as previously published (59), results in selective transduction of single-layered surface ectoderm of living E9.5 mouse embryos. Lentiviral vectors with Scramble (not targeting) shRNAs and constitutive expression [phosphoglycerate kinase (PGK) promoter-driven] of H2B-RFP were previously reported (59). We modified these pLKO.1-based vectors to replace the PGK promoter with a newly assembled tetracycline regulatory enhancer (TRE) promoter sequence (based on TRE3G from Clontech). We cloned sensor and mRFP-K10 genes from pMAX vectors into pLKO.1-based vectors, downstream of the TRE. Using these pLKO.1 vectors, we generated high-titer viruses in 293FT cells as previously described (59). To induce expression of TRE-controlled genes in vivo, we fed females fostering lentivirally transduced embryos with doxycycline.

For knockdown of mouse filaggrin, we identified hairpins with high intrinsic scores and no predicted off-targets using the GPP Web Portal (https://portals.broadinstitute.org/gpp/public/). We modified our lentiviral vectors harboring H2B-RFP to substitute their Scramble shRNA with hairpins against (mouse) Flg (#01: with target sequence ATCAATCTCACAGCTATTATT localized to the C-terminal domain, and #02: with target sequence CTCCGGATTCTACCCAGTATA within the filaggrin repeats). We tested both hairpins in mouse skin and they efficiently depleted mFLG and its KGs (Fig. 7 shows data for hairpin #02). To transduce human primary keratinocytes with lentiviral vectors harboring H2B-RFP and phase-separation sensors, we used neonatal and adult human primary keratinocytes that we purchased from Life Technologies. We transduced them by exposing them briefly to the corresponding high titer lentiviruses diluted in supplemented Epilife media (Thermo Fisher Scientific). A similar lentiviral transduction approach was used to generate HaCATs with doxycycline-inducible expression of mRFP-K10. See supplementary materials and methods for detailed protocols.

Live imaging

For live imaging of mouse skin, we harvested head skin from E18.5 mouse embryos that were in utero transduced as explained above. After removing the skin from the embryos, we gently scraped off the fat leaving the dermis intact, cut out 1-cm^2 pieces and placed them with the stratum corneum facing down on a glass-bottom 35-mm dish (MatTek) and on top of Phenol-red free growth-factor reduced matrigel (Corning). We pressed the tissue flat against the glass surface using a transparent porous membrane (Whatman Nuclepore Track-Etched Membranes, 13-mm diameter, 5-μm pores) and a 12-mm cover glass (Fisherbrand). Once the tissue was flat, we removed the cover glass and allowed the matrigel to solidify at 37°C for 15 min. We then added CnT-Prime Airlift, Full Thickness Skin Airlift Medium (from CELLnTEC), typically supplemented with 2 μg/ml doxycycline. We imaged these samples using a spinning-disk microscope equipped with a 40× oil objective and a live imaging chamber with a constant supply of CO_2 and maintained at 37°C. We imaged with up to two lasers (488 and 561 nm, at 5.2 mW) and with exposure times of 200 ms per laser. We obtained full z stacks of the suprabasal epidermis every 20 min (to limit phototoxicity) for 16 to 20 hours. For photobleaching experiments of sensor-labeled KGs in mouse skin, we followed the procedure previously described for the analysis of sensor recovery half-lives in culture. For pH-shift experiments, we first isolated the epidermal skin layer by dispase treatment of E18.5 whole skin. The tissue was mounted with the stratum corneum facing upward in an otherwise identical manner to the approach described for imaging of whole skin. The tissue was initially imaged using CnT-Airlift media (pH 7.4) before adding an equal volume of acidic CnT-Airlift media (regular media but supplemented for buffering of intracellular pH by adding 280 mM KCl, 20 mM nigericin and HCl to reach a pH of ~3.3) to set the final media pH to ~6.2 to 6.4. Upon the pH shift, the tissue was imaged every 5 min for 50 min under usual live imaging conditions. For pH-shift experiments with primary human keratinocytes, we used the same approach as described for mouse epidermis. For HaCATs with engineered KGs, we performed the pH-shift experiments as before, but with acidic CnT-PR-D supplemented with 1.5 mM $CaCl_2$. Live imaging data of the thick epidermis were typically presented and analyzed from 3D projections of the raw (without rendering) fluorescent data. These 3D views and additional surface renderings were built using Imaris software (version 8.3.1). For live imaging of cells in culture, we typically presented (and indicated so in the legends) maximum intensity projections prepared with ImageJ.

Selection and synthesis of pH reporters

For the synthesis of genetically encoded pH reporters that sensitively respond with a pK_a near 6.5, we chose two previously published and well-characterized pH reporters: SEpHLuorin (60) and mNectarine (61). We PCR-amplified genes encoding these proteins from Addgene plasmids (#58500 and #80151, respectively) and cloned them into pMAX vectors downstream of a cytomegalovirus (CMV) promoter. For expression of pH reporters in mouse skin throughout epidermal differentiation, we subcloned genes encoding pH reporters into our TRE3G-driven pLKO.1-based vectors and lentivirally transduced embryonic mouse skin as in our previous experiments. We note that these pH reporters are not ratiometric and do not report absolute pH but rather relative changes in pH. However, because we use them for live imaging, we can confidently identify relative changes in intracellular pH by comparing changes in reporter fluorescence within individual cells over time. This approach accounts for the intrinsic limitation of nonratiometric pH reporters—namely, that the total fluorescent signal varies based on expression levels at the single-cell level. In our approach, rapid changes in fluorescent signal are interpreted as relative changes in pH by correcting for the intensity of the reporter within each cell in time points immediately before the event. Addgene plasmid # 58500 was a gift from A. Cohen. Addgene plasmid # 80151 was a gift from S. Di Pietro.

Design and synthesis of conventional client proteins for KGs

FLG variants that are uniquely bound (with low affinity) by conventional clients were synthesized as part of pMAX vectors and as previously described for other FLG repeat proteins —see their full sequences in table S5. Briefly, these filaggrin scaffold proteins carry short unique domains recognized by the client (either the cleavage sequence for TEV protease or the murine S100 domain). Genes encoding clients were synthesized as IDT gblocks and cloned into pMAX vectors using the same cloning approach as previously described for phase separation sensors. The sequence details of each client, either a dead-variant of Tobacco Etch Virus Protease (dTEVP) or a mS100 domain, are also included in table S5. Although the dTEVP client was exclusively studied in immortalized human keratinocytes (using transfection of corresponding pMAX vectors), for the mS100-based client, which has affinity for endogenous mouse filaggrin, we also subcloned genes encoding this client into our TRE3G-driven pLKO.1-based vectors for lentiviral transduction of the embryonic murine epidermis.

Immunofluorescence of fixed cells and tissues

To prepare HaCATs for immunostaining, we fixed cultures at 37°C for 10 min using 4% paraformaldehyde in Dulbecco's phosphate-buffered saline (DPBS). Cultures were washed with DPBS and stored at 4°C before immunostaining. To prepare murine skin for wholemount immunostaining, we treated whole skin with dispase for 30 min at 37°C to isolate the epidermis. We fixed the epidermis at 37°C for 30 min in 4% paraformaldehyde. After subsequent washes in DPBS, we stored the tissue at 4°C in DPBS before immunostaining. In all cases, we permeabilized the tissue with an antibody blocking buffer for 3 to 4 hours before overnight incubation with primary antibodies. The following primary antibodies were used: chicken anti-GFP (1:2000, Abcam), rabbit anti-RPTN (1:200, Sigma HPA030483), rabbit anti-mFLG (1:1000, Fuchs Lab), rabbit anti-mFLG (1:1000, Abcam ab24584), and goat anti-hFLG (1:200, Santa Cruz, sc-25897). After washing with DPBS, we added species-specific secondary antibodies conjugated to RRX or AF647 and incubated the cultures and tissues for 4 hours at room temperature. After washing with DAPI, the samples were mounted with ProLong Gold Antifade Mountant (Invitrogen) and cured overnight before imaging. For filaggrin immunostaining without secondary antibodies (i.e., direct detection) in mouse skin, we first conjugated anti-mFLG (abcam) to AF647 using an Alexa Fluor 647 Antibody Labeling Kit (ThermoFisher) and following the instructions of the manufacturer. Cultured cells and whole-mounted fixed tissues were imaged using a spinning-disk microscope equipped with a 40× oil objective. Images were analyzed using ImageJ and Imaris 8.3.1.

Skin barrier assay

To measure barrier quality, we obtained transepidermal water loss measurements (TEWL) using a Tewameter TM 300 (Courage + Khazaka electronic GmbH) on explanted neonatal back skin. Briefly, neonates were humanely sacrificed and their back skin was harvested and immediately spread over a clean surface. We collected four TEWL measurements per sample on fully acclimatized skin. The values reported by the instrument were not further processed and corresponded to grams of lost water per hour per m^2 of skin. We measured two or three animals in three independent experiments.

Statistical analyses

Whenever we indicate statistical significance, these are cases where we reject, with a confidence greater than 0.05 (i.e., $p < 0.05$) the null hypothesis that the difference in the mean values between two datasets is equal to zero. To perform this hypothesis testing, we ran two-sample t tests using OriginPro. In all cases, we verified that the statistical differences did not depend on the assumption of equal variance (Welch-correction) between samples.

Supplementary Material

Refer to Web version on PubMed Central for supplementary material.

ACKNOWLEDGMENTS

We thank I. Matos for assistance with the live-imaging setup; L. Hidalgo and M. Sribour for animal assistance; and S. Ellis and I. Matos for discussion and comments on the manuscript. We thank the Molecular Cytology Core Facility at MSKCC and Rockefeller University (RU) Bio-Imaging Resource Center for use of microscopes, and RU Comparative Bioscience Center (AAALAC-accredited) for care of micein accordance with National Institutes of Health (NIH) guidelines.

Funding: This work was funded by NIH (R01-AR27883 to E.F.) and partly supported by the Robertson Therapeutic Development Fund and by a Tri-Institutional Starr Stem Cell Scholars Fellowship at The Rockefeller University. E.F. is an HHMI investigator. F.G.Q. holds a Career Award at the Scientific Interface from Burroughs Wellcome Fund.

REFERENCES AND NOTES

1. Brangwynne CP et al., Germline P granules are liquid droplets that localize by controlled dissolution/condensation Science 324, 1729–1732 (2009). doi: 10.1126/science.1172046 [PubMed: 19460965]
2. Banani SF, Lee HO, Hyman AA, Rosen MK, Biomolecular condensates: Organizers of cellular biochemistry. Nat. Rev. Mol. Cell Biol 18, 285–298 (2017). doi: 10.1038/nrm.2017.7 [PubMed: 28225081]
3. Shin Y, Brangwynne CP, Liquid phase condensation in cell physiology and disease. Science 357, eaaf4382 (2017).doi: 10.1126/science.aaf4382 [PubMed: 28935776]
4. Feric M et al., Coexisting liquid phases underlie nucleolar subcompartments. Cell 165, 1686–1697 (2016). doi: 10.1016/j.cell.2016.04.047 [PubMed: 27212236]
5. Su X et al., Phase separation of signaling molecules promotes T cell receptor signal transduction. Science 352, 595–599 (2016). doi: 10.1126/science.aad9964 [PubMed: 27056844]
6. Wang JT et al., Regulation of RNA granule dynamics by phosphorylation of serine-rich, intrinsically disordered proteins in C. elegans. eLife 3, e04591 (2014). doi: 10.7554/eLife.04591 [PubMed: 25535836]
7. Molliex A et al., Phase separation by low complexity domains promotes stress granule assembly and drives pathological fibrillization. Cell 163, 123–133 (2015). doi: 10.1016/j.cell.2015.09.015 [PubMed: 26406374]
8. Sabari BR et al., Coactivator condensation at super-enhancers links phase separation and gene control. Science 361, eaar3958 (2018). doi: 10.1126/science.aar3958 [PubMed: 29930091]
9. Cho W-K et al., Mediator and RNA polymerase II clusters associate in transcription-dependent condensates. Science 361, 412–415 (2018). doi: 10.1126/science.aar4199 [PubMed: 29930094]
10. Gibson BA et al., Organization of chromatin by intrinsic and regulated phase separation. Cell 179, 470–484.e21 (2019). doi: 10.1016/j.cell.2019.08.037 [PubMed: 31543265]
11. Wan G et al., Spatiotemporal regulation of liquid-like condensates in epigenetic inheritance. Nature 557, 679–683 (2018). doi: 10.1038/s41586-018-0132-0 [PubMed: 29769721]
12. Lin Y, Protter DS, Rosen MK, Parker R, Formation and maturation of phase-separated liquid droplets by RNA-binding proteins. Mol. Cell 60, 208–219 (2015). doi: 10.1016/j.molcel.2015.08.018 [PubMed: 26412307]
13. Jiang H et al., Phase transition of spindle-associated protein regulate spindle apparatus assembly. Cell 163, 108–122 (2015). doi: 10.1016/j.cell.2015.08.010 [PubMed: 26388440]
14. Rai AK, Chen J-X, Selbach M, Pelkmans L, Kinase-controlled phase transition of membraneless organelles in mitosis. Nature 559, 211–216 (2018). doi: 10.1038/s41586-018-0279-8 [PubMed: 29973724]
15. Beutel O, Maraspini R, Pombo-García K, Martin-Lemaitre C, Honigmann A, Phase Separation of Zonula Occludens Proteins Drives Formation of Tight Junctions. Cell 179, 923–936.e11 (2019). doi: 10.1016/j.cell.2019.10.011 [PubMed: 31675499]
16. Freeman Rosenzweig ES et al., The eukaryotic CO2-concentrating organelle is liquid-like and exhibits dynamic reorganization. Cell 171, 148–162.e19 (2017). doi: 10.1016/j.cell.2017.08.008 [PubMed: 28938114]
17. Alberti S, Gladfelter A, Mittag T, Considerations and Challenges in Studying Liquid-Liquid Phase Separation and Biomolecular Condensates. Cell 176, 419–434 (2019).doi: 10.1016/j.cell.2018.12.035 [PubMed: 30682370]
18. Schmidt HB, Barreau A, Rohatgi R, Phase separation-deficient TDP43 remains functional in splicing. Nat. Commun 10, 4890 (2019). doi: 10.1038/s41467-019-12740-2 [PubMed: 31653829]
19. Bracha D et al., Mapping Local and Global Liquid Phase Behavior in Living Cells Using Photo-Oligomerizable Seeds. Cell 175, 1467–1480.e13 (2018). doi: 10.1016/j.cell.2018.10.048 [PubMed: 30500534]
20. Segre JA, Epidermal barrier formation and recovery in skin disorders. J. Clin. Invest 116, 1150–1158 (2006). doi: 10.1172/JCI28521 [PubMed: 16670755]

21. Dale BA, Resing KA, Presland RB, in The Keratinocyte Handbook, Leigh I, Lane EB, Watt FM, Eds. (Cambridge Univ. Press, 1994), chap. 17, pp. 323–350.
22. Quiroz FG, Chilkoti A, Sequence heuristics to encode phase behaviour in intrinsically disordered protein polymers. Nat. Mater 14, 1164–1171 (2015). doi: 10.1038/nmat4418 [PubMed: 26390327]
23. Palmer CN et al., Common loss-of-function variants of the epidermal barrier protein filaggrin are a major predisposing factor for atopic dermatitis. Nat. Genet 38, 441–446 (2006). doi: 10.1038/ng1767 [PubMed: 16550169]
24. Brown SJ, McLean WH, One remarkable molecule: Filaggrin. J. Invest. Dermatol 132, 751–762 (2012). doi: 10.1038/jid.2011.393 [PubMed: 22158554]
25. Margolis DJ et al., Filaggrin-2 variation is associated with more persistent atopic dermatitis in African American subjects. J. Allergy Clin. Immunol 133, 784–789 (2014). doi: 10.1016/j.jaci.2013.09.015 [PubMed: 24184149]
26. Rahrig S et al., Transient epidermal barrier deficiency and lowered allergic threshold in filaggrin-hornerin (FlgHrnr$^{-/-}$) double-deficient mice. Allergy 74, 1327–1339 (2019). doi: 10.1111/all.13756 [PubMed: 30828807]
27. Wong XFCC et al., Array-based sequencing of filaggrin gene for comprehensive detection of disease-associated variants. J. Allergy Clin. Immunol 141, 814–816 (2018). doi: 10.1016/j.jaci.2017.10.001 [PubMed: 29056476]
28. Lo C-A et al., Quantification of protein levels in single living cells. Cell Rep. 13, 2634–2644 (2015). doi: 10.1016/j.celrep.2015.11.048 [PubMed: 26686644]
29. Bunick CG et al., Crystal structure of human profilaggrin S100 domain and identification of target proteins annexin II, stratifin, and HSP27. J. Invest. Dermatol 135, 1801–1809 (2015). doi: 10.1038/jid.2015.102 [PubMed: 25760235]
30. Banani SF et al., Compositional control of phase-separated cellular bodies. Cell 166, 651–663 (2016). doi: 10.1016/j.cell.2016.06.010 [PubMed: 27374333]
31. Schuster BS et al., Controllable protein phase separation and modular recruitment to form responsive membraneless organelles. Nat. Commun 9, 2985 (2018). doi: 10.1038/s41467-018-05403-1 [PubMed: 30061688]
32. Christensen T, Hassouneh W, Trabbic-Carlson K, Chilkoti A, Predicting transition temperatures of elastin-like polypeptide fusion proteins. Biomacromolecules 14, 1514–1519 (2013). doi: 10.1021/bm400167h [PubMed: 23565607]
33. McNaughton BR, Cronican JJ, Thompson DB, Liu DR, Mammalian cell penetration, siRNA transfection, and DNA transfection by supercharged proteins. Proc. Natl. Acad. Sci. U.S.A 106, 6111–6116 (2009). doi: 10.1073/pnas.0807883106 [PubMed: 19307578]
34. Jaubert J, Patel S, Cheng J, Segre JA, Tetracycline-regulated transactivators driven by the involucrin promoter to achieve epidermal conditional gene expression. J. Invest. Dermatol 123, 313–318 (2004). doi: 10.1111/j.0022-202X.2004.23203.x [PubMed: 15245431]
35. Bonnart C et al., Elastase 2 is expressed in human and mouse epidermis and impairs skin barrier function in Netherton syndrome through filaggrin and lipid misprocessing. J. Clin. Invest 120, 871–882 (2010). doi: 10.1172/JCI41440 [PubMed: 20179351]
36. Rompolas P et al., Spatiotemporal coordination of stem cell commitment during epidermal homeostasis. Science 352, 1471–1474 (2016). doi: 10.1126/science.aaf7012 [PubMed: 27229141]
37. Kartasova T, Roop DR, Holbrook KA, Yuspa SH, Mouse differentiation-specific keratins 1 and 10 require a preexisting keratin scaffold to form a filament network. J. Cell Biol 120, 1251–1261 (1993). doi: 10.1083/jcb.120.5.1251 [PubMed: 7679677]
38. Kumar V et al., A keratin scaffold regulates epidermal barrier formation, mitochondrial lipid composition, and activity. J. Cell Biol 211, 1057–1075 (2015). doi: 10.1083/jcb.201404147 [PubMed: 26644517]
39. Lee C-H, Kim M-S, Chung BM, Leahy DJ, Coulombe PA, Structural basis for heteromeric assembly and perinuclear organization of keratin filaments. Nat. Struct. Mol. Biol 19, 707–715 (2012). doi: 10.1038/nsmb.2330 [PubMed: 22705788]
40. Hughes MP et al., Atomic structures of low-complexity protein segments reveal kinked b sheets that assemble networks. Science 359, 698–701 (2018). doi: 10.1126/science.aan6398 [PubMed: 29439243]

41. Noda S et al., The Asian atopic dermatitis phenotype combines features of atopic dermatitis and psoriasis with increased TH17 polarization. J. Allergy Clin. Immunol 136, 1254–1264 (2015). doi: 10.1016/j.jaci.2015.08.015 [PubMed: 26428954]
42. Nott TJ et al., Phase transition of a disordered nuage protein generates environmentally responsive membraneless organelles. Mol. Cell 57, 936–947 (2015). doi: 10.1016/j.molcel.2015.01.013 [PubMed: 25747659]
43. Dzuricky M, Roberts S, Chilkoti A, Convergence of artificial protein polymers and intrinsically disordered proteins. Biochemistry 57, 2405–2414 (2018). doi: 10.1021/acs.biochem.8b00056 [PubMed: 29683665]
44. Niesner R et al., 3D-resolved investigation of the pH gradient in artificial skin constructs by means of fluorescence lifetime imaging. Pharm. Res 22, 1079–1087 (2005). doi: 10.1007/s11095-005-5304-6 [PubMed: 16028008]
45. Mackay JA, Callahan DJ, Fitzgerald KN, Chilkoti A, Quantitative model of the phase behavior of recombinant pH-responsive elastin-like polypeptides. Biomacromolecules 11, 2873–2879 (2010). doi: 10.1021/bm100571j [PubMed: 20925333]
46. Alberti S, Guilty by association: Mapping out the molecular sociology of droplet compartments. Mol. Cell 69, 349–351 (2018). doi: 10.1016/j.molcel.2018.01.020 [PubMed: 29395058]
47. Markmiller S et al., Context-dependent and disease-specific diversity in protein interactions within stress granules. Cell 172, 590–604.e13 (2018). doi: 10.1016/j.cell.2017.12.032 [PubMed: 29373831]
48. Brody I, An ultrastructural study on the role of the keratohyalin granules in the keratinization process. J. Ultrastruct. Res 3, 84–104 (1959). doi: 10.1016/S0022-5320(59)80018-6 [PubMed: 13804667]
49. Makino T, Takaishi M, Morohashi M, Huh NH, Hornerin, a novel profilaggrin-like protein and differentiation-specific marker isolated from mouse skin. J. Biol. Chem 276, 47445–47452 (2001). doi: 10.1074/jbc.M107512200 [PubMed: 11572870]
50. Steinert PM, Parry DA, Marekov LN, Trichohyalin mechanically strengthens the hair follicle: Multiple cross-bridging roles in the inner root shealth. J. Biol. Chem 278, 41409–41419 (2003). doi: 10.1074/jbc.M302037200 [PubMed: 12853460]
51. Mészáros B et al., PhaSePro: The database of proteins driving liquid–liquid phase separation. Nucleic Acids Res. 48, D360–D367 (2020). doi: 10.1093/nar/gkz848 [PubMed: 31612960]
52. Kyte J, Doolittle RF, A simple method for displaying the hydropathic character of a protein. J. Mol. Biol 157, 105–132 (1982). doi: 10.1016/0022-2836(82)90515-0 [PubMed: 7108955]
53. McDaniel JR, Mackay JA, Quiroz FG, Chilkoti A, Recursive directional ligation by plasmid reconstruction allows rapid and seamless cloning of oligomeric genes. Biomacromolecules 11, 944–952 (2010). doi: 10.1021/bm901387t [PubMed: 20184309]
54. Woerner AC et al., Cytoplasmic protein aggregates interfere with nucleocytoplasmic transport of protein and RNA. Science 351, 173–176 (2016). doi: 10.1126/science.aad2033 [PubMed: 26634439]
55. Boudko SP et al., Crystal structure of human collagen XVIII trimerization domain: A novel collagen trimerization Fold. J. Mol. Biol 392, 787–802 (2009). doi: 10.1016/j.jmb.2009.07.057 [PubMed: 19631658]
56. Ghoorchian A, Holland NB, Molecular architecture influences the thermally induced aggregation behavior of elastin-like polypeptides. Biomacromolecules 12, 4022–4029 (2011). doi: 10.1021/bm201031m [PubMed: 21972921]
57. Maas-Szabowski N, Stärker A, Fusenig NE, Epidermal tissue regeneration and stromal interaction in HaCaT cells is initiated by TGF-a. J. Cell Sci 116, 2937–2948 (2003). doi: 10.1242/jcs.00474 [PubMed: 12771184]
58. Nowak JA, Fuchs E, in Stem Cells in Regenerative Medicine. (Springer, 2009), pp. 215–232.
59. Beronja S, Livshits G, Williams S, Fuchs E, Rapid functional dissection of genetic networks via tissue-specific transduction and RNAi in mouse embryos. Nat. Med 16, 821–827 (2010). doi: 10.1038/nm.2167 [PubMed: 20526348]

60. Sankaranarayanan S, De Angelis D, Rothman JE, Ryan TA, The use of pHluorins for optical measurements of presynaptic activity. Biophys. J 79, 2199–2208 (2000). doi: 10.1016/S0006-3495(00)76468-X [PubMed: 11023924]

61. Johnson DE et al., Red fluorescent protein pH biosensor to detect concentrative nucleoside transport. J. Biol. Chem 284, 20499–20511 (2009). doi: 10.1074/jbc.M109.019042 [PubMed: 19494110]

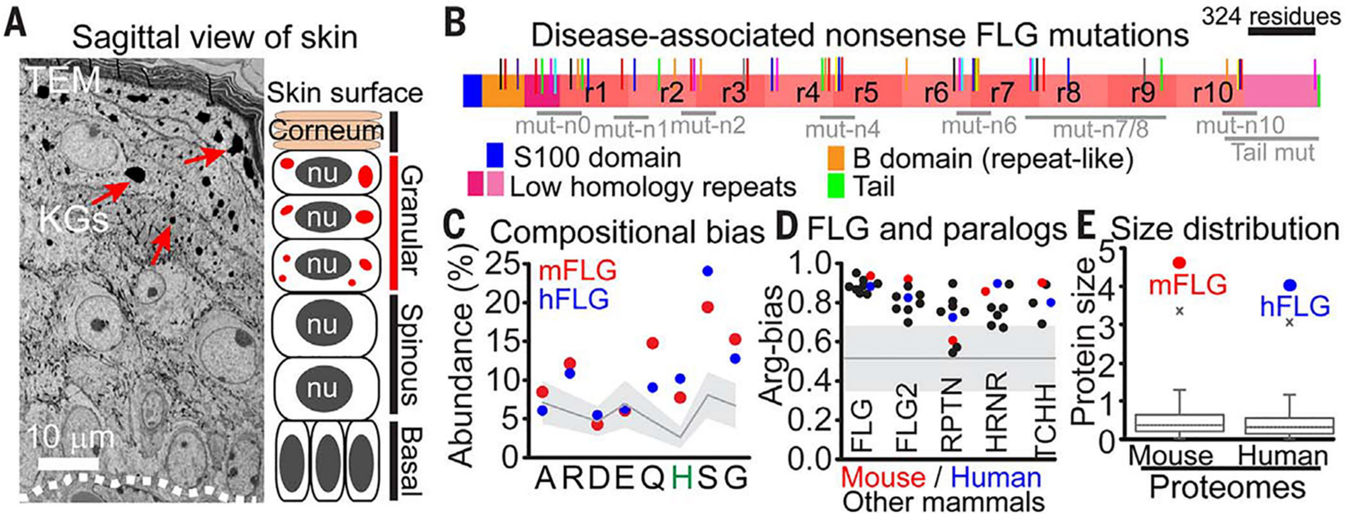

Fig. 1. Filaggrin family proteins have phase-separation characteristics, and their mutations are linked to human skin barrier disorders.

(A) Ultrastructure and schematic of mouse skin at E17.5. Dotted lines delineate the basement membrane, where proliferative epidermal progenitors attach (basal layer). Periodically, progenitors initiate terminal differentiation, ceasing to divide, but transcribe the necessary genes for skin barrier formation as they flux upward through keratin filament bundle–rich spinous layers; keratohyalin granule (KGs, arrows)-rich granular layers; and dead, enucleated squames, which continually slough from the skin surface (corneum), replenished by differentiating cells from beneath. nu, nucleus. **(B)** Domain architecture of human FLG, the major known constituent of KGs, and location of nonsense FLG mutations (colored lines) associated with skin barrier disorders (fig. S1 shows mutants). Many mutations cluster to generate truncated variants in FLG repeat domains (labeled as mut-n0 to mut-n10). **(C)** Mouse and human FLG are histidine-rich, low-complexity (LC) proteins with identical biases in amino acid composition, but not sequence. Mean amino acid abundance across the human proteome is shown as a gray line (filled area is the standard deviation). Amino acid abbreviations: A, Ala; R, Arg; D, Asp; E, Glu; Q, Gln; H, His; S, Ser; G, Gly. **(D)** FLG and its paralogs (FLG2, RPTN, HRNR, and TCHH) share a strong preference for arginine over lysine residues [calculated as R/(R+K)], a major determinant of phase separation in LC proteins (22). The gray line marks the mean Arg bias across the mouse and human proteome (filled area is the standard deviation). See fig. S3 for details. **(E)** Proteome-wide distribution of protein size (unit length 1000 amino acids), underscoring the enormous size of FLG (x marks the 99th percentile).

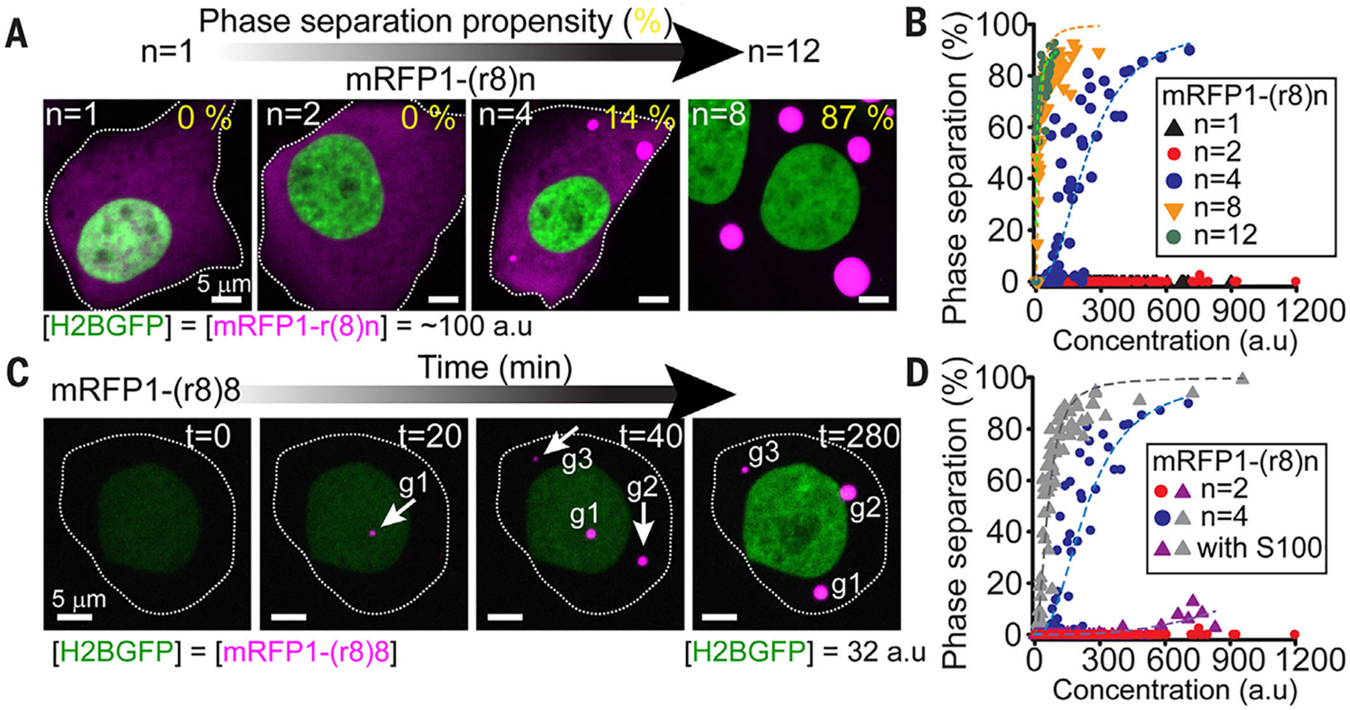

Fig. 2. Filaggrin proteins undergo liquid-liquid phase transitions that are disrupted by disease-associated filaggrin mutations.

(A) Transfection of synthesized FLG genes into HaCATs reveals that the propensity of FLG repeat proteins to undergo phase separation is governed by the number of FLG repeats. In these experiments, genes encoding tagged-FLG variants [mRFP-(r8)n, where r8 = repeat #8 and n = 1 to 8 of these repeats] were fused C-terminal to a H2B-GFP-(p2a) construct. Cotranslationally, the self-cleavable (p2a) sequence (28) ensures that each construct generates one H2B-GFP molecule for each mRFP-(r8)n molecule. Panels show cells with the same total concentration of mRFP-(8)n. Quantitatively, phase-separation propensity was defined as the percentage of total mRFP signal within phase-separated granules. **(B)** Phase-separation propensity for FLG variants spanning the repeat distribution of truncated FLG mutants (mut-n0 to mut-n8 in Fig. 1B; WT-size is n =12) and across a wide range of expression levels for each variant. Dashed lines are logistic fits to data with signs of a concentration-dependent phase transition. **(C)** Time-lapse imaging of HaCATs expressing increasing amounts of mRFP-(r8)8 [related to H2BGFP via (p2a)]. Shown are the initial stages of phase separation through the formation and growth of granules (marked as g1 to g3). **(D)** The S100 (dimerization) domain of human FLG enhances the phase-separation propensity of FLG repeat proteins but fails to rescue phase behavior in disease-associated variants with ≤2 FLG repeats (mut-n0-n2 in Fig. 1B). Construct design and quantifications are as in (B). Dashed lines are logistic fits to the data. Images are maximum intensity projections.

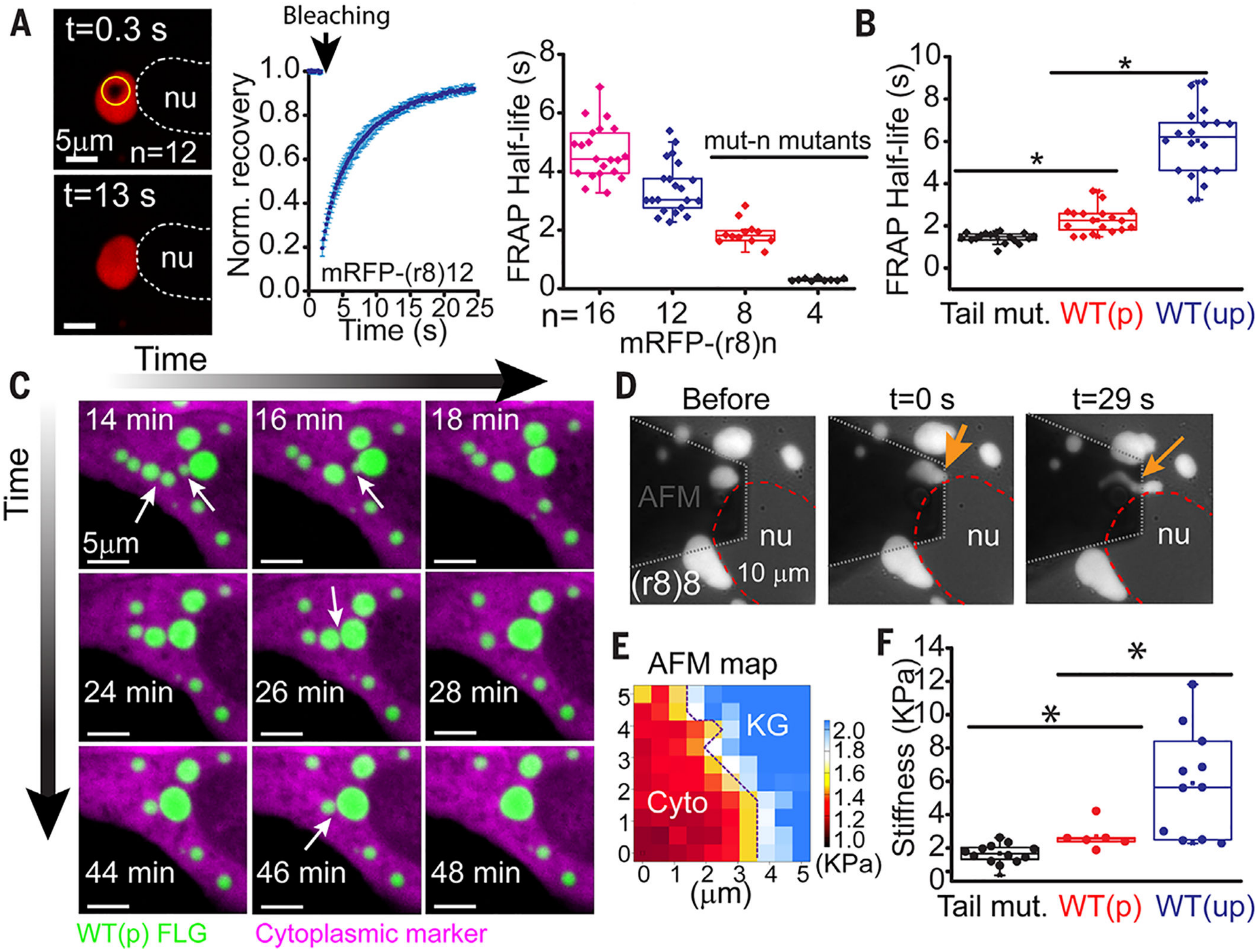

Fig. 3. Filaggrin-processing and disease-associated mutations alter the liquid-like behavior and material properties of KG-like membraneless compartments.

(A) FRAP half-lives of granules formed de novo in immortalized human keratinocytes after transfection of indicated mRFP1-tagged FLGs with different FLG repeat truncations. Left: Representative images of a recovery event; middle: representative FRAP recovery plot (average ± SD from seven granules); right: quantifications. (B) FRAP half-lives after internal photobleaching of granules formed from a mRFP-FLG [WT(p), mRFP-(r8)8-Tail] in comparison to one that either lacks the 26–amino acid tail domain (Tail mut) or contains the amino (S100) domain of FLG [WT(up)]. Each symbol in (A) and (B) represents an individual FRAP half-life measurement of granules from multiple cells. Data are from ≥2 experiments. **(C)** Tagged-FLG granules undergo liquid-like fusion events. Live imaging of a cell transfected with a cytoplasmic marker (mCherry) and a WT(p) FLG [sfGFP-r(8) 12-Tail]. Arrows point to granule fusion events over time (movie S1). **(D to F)** Atomic force microscopy (AFM) reveals liquid-like behaviors of granules. (D) Snapshots of granule (arrows) before and with pressure application reveal liquid-like streaming behavior (movie S3). (E) Representative AFM map shows that even KGs composed of the FLG tail mutant appear to be stiffer than cytoplasm (see fig. S10 for WT-type KGs data). (F) Average stiffness (Young’s modulus) per granule for KGs assembled from the FLG variants described in (B). Each dot corresponds to measurements of a different granule (average of all pixels within the granule domain in the stiffness map) in a different cell. nu, nucleus; asterisks, statistically significant ($p < 0.05$).

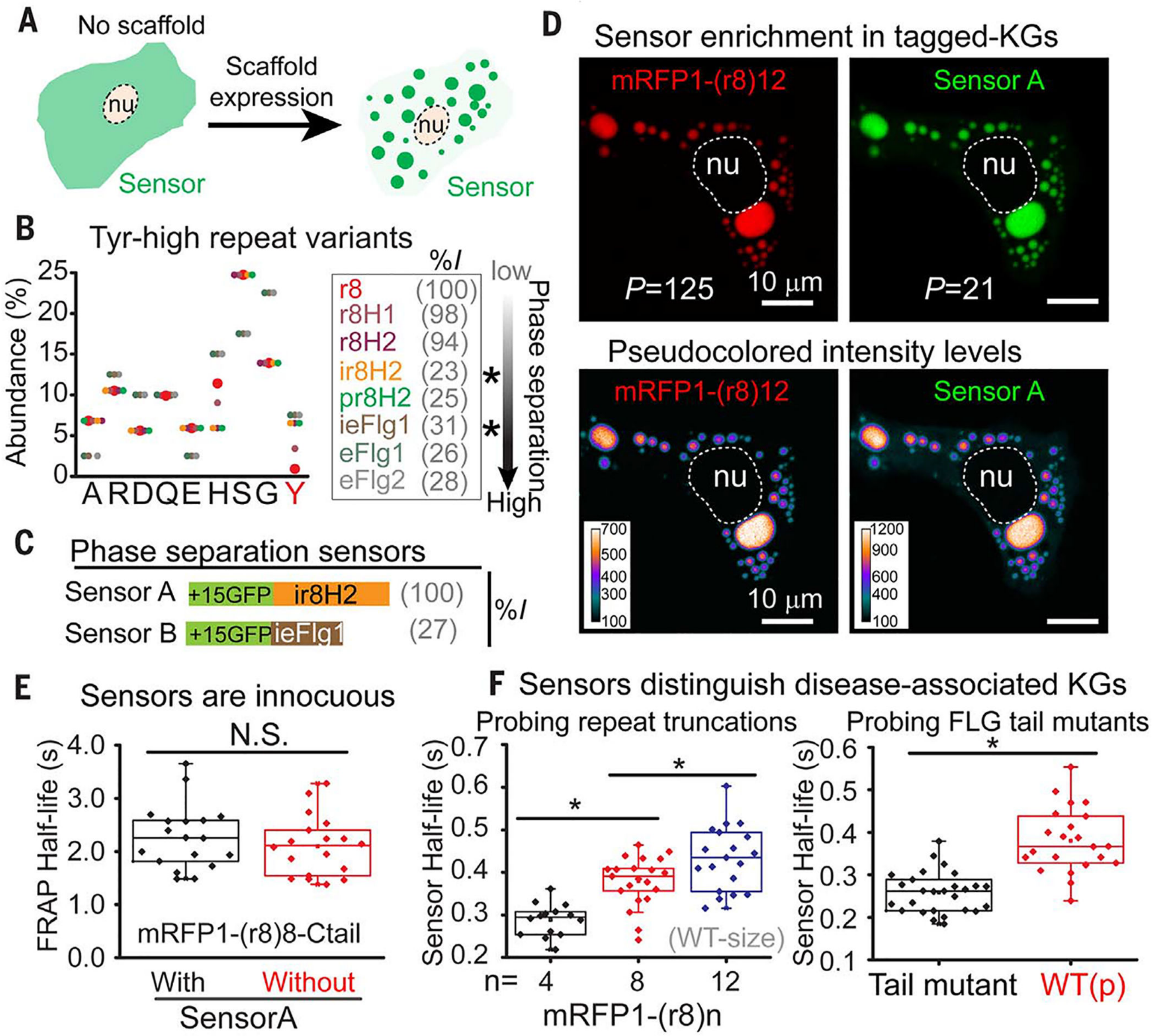

Fig. 4. Phase-separation sensors efficiently enter and detect KGs and accurately report their liquid-like properties.

(A) Concept of a genetically encoded phase-separation sensor. **(B)** Amino acid composition of LC Tyr-high variants of a FLG repeat (repeat 8, r8), ordered at right according to phase-separation propensity. Variants were generated according to nonpathogenic residues frequently altered in FLG repeats in humans. %I: percent sequence identity to WT FLG repeat. Asterisks denote the two Tyr-high variants used as phase sensors in this study. Y, Tyr. **(C)** Domain architecture of the two phase-separation sensors. %I: percent sequence identity to sensor A. **(D)** Sensor partitioning into KGs in HaCATs expressing sensor A and indicated mRFP1-FLG. Partition coefficients (P, ratio of background-corrected signal inside and outside granules) reveal robust ability of sensor A to recognize FLG in its phase-separated granules (bottom row is pseudocolored to reveal the range of fluorescent intensity values).

nu, nucleus. **(E)** Presence of sensor A does not alter FRAP half-life of FLG-assembled KGs in HaCATs. N.S., not statistically significant. **(F)** Sensor A recovery half-lives after photobleaching granules composed of the indicated mRFP1-tagged FLG variants that model patient mutations. Each symbol in (E) and (F) represents an individual FRAP half-life measurement of granules from multiple cells. Data are from ≥2 experiments. Asterisks, statistically significant ($p < 0.05$). See also related figs. S11 to S14.

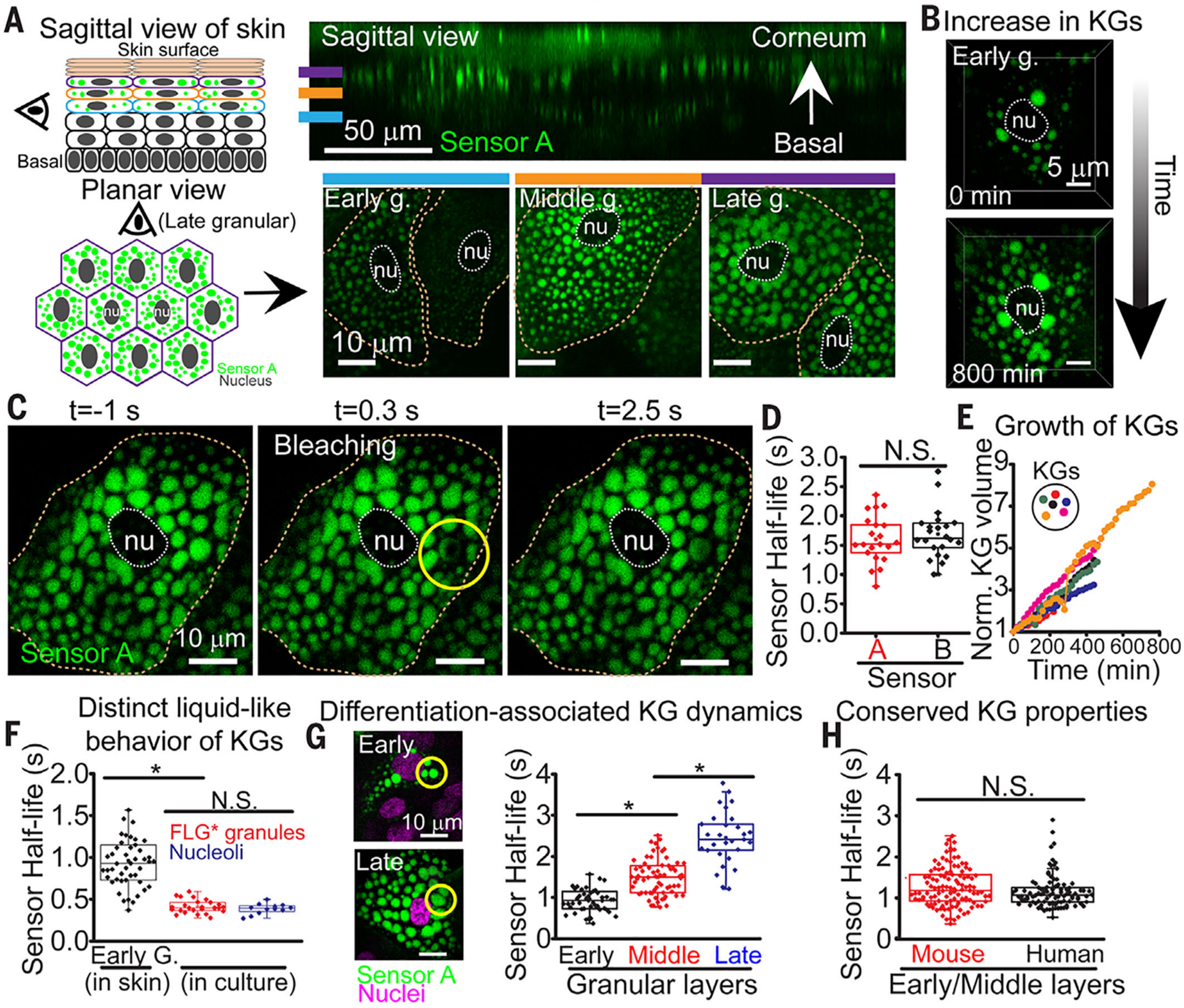

Fig. 5. Skin exhibits pronounced phase separation dynamics during barrier formation.

(A) (Left) Schematics of sagittal and planar views. (Right) Corresponding views of fluorescent sensor A in mouse skin. Planar skin views are through early, middle, and late granular layers. nu, nucleus. Dotted lines denote cell boundaries. **(B)** Live imaging of an early granular cell over 800 min. **(C)** Example of photobleaching the sensor A signal within a KG of a granular cell in mouse skin. **(D)** Sensor recovery half-lives after photobleaching KGs across cells within mid-granular layer of transduced mouse skin (each point is from a different cell; two animals analyzed per sensor). **(E)** Quantification of changes in KG volume over time in cells as they reach the upper granular layer (related to movie S6). **(F)** Sensor A reveals distinct liquid phase properties within different biomolecular condensates and contexts [in vivo KGs versus granules generated de novo from S100-mRFP-(r8)8-Tail, expressed in cultured keratinocytes]. For nucleolar measurements, a sensor A variant lacking a nuclear export signal was used. In vivo and in vitro data from ≥2 experiments. **(G)** Sensor

A detects an increase in relative KG viscosity that occurs during granular layer maturation. Shown are FRAP half-lives in KGs within different granular layers (morphological differences at left; data from three animals). **(H)** Sensor A reveals conserved liquid-like KG properties despite divergence in amino acid sequence of granule-forming proteins. Mouse KG data in (H) are same as in (G). Human KG data are from three skin equivalents and two sources of primary human keratinocytes. Asterisks, statistically significant ($p < 0.05$). N.S., not significant.

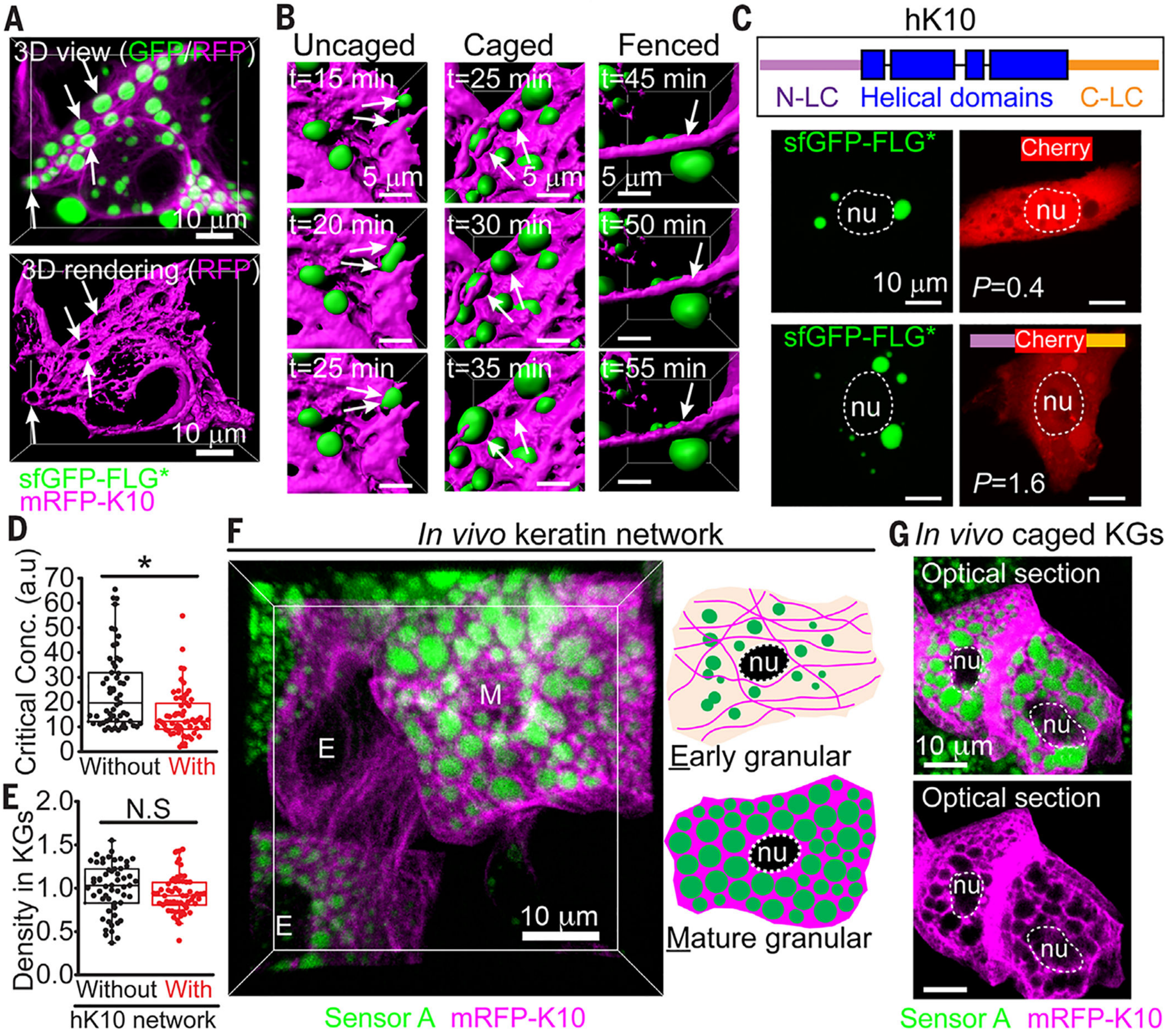

Fig. 6. Keratin-FLG interactions stabilize KGs and structure the cytoplasm in skin.

(A) HaCATs were induced to express mRFP1-K10, which integrates into the endogenous K5/K14 filaments. Cells were then transfected with sfGFP-FLG*, which formed liquid-like KGs (arrows) interspersed within the keratin network. Top: 3D projections of GFP/RFP; bottom: surface rendering of mRFP-K10. **(B)** Live imaging of cell in (A), showing surface rendering of three different types of keratin-KG interactions (see fig. S18A for maximum intensity projections). Uncaged KGs fuse rapidly; caged KGs fuse rarely or slowly; fenced KGs are impeded from fusing. Double arrows depict temporal fusion events; single arrow denotes keratin cable preventing fusion. **(C)** When mCherry harbors hK10 LC domains, it partially partitions into KGs (P = 1.6). **(D)** Phase separation of sfGFP-(r8)4 FLG is promoted in HaCATs displaying mRFP1-K10 fibers. Critical concentrations for phase separation were estimated as in fig. S7C (data from three experiments). **(E)** FLG density within KGs assembled in (D) is similar ± an hK10 network. **(F)** Planar 3D view of E18.5 granular layer from skin of an embryo transduced in utero with a suprabasal-specific driver of mRFP1-K10 and sensor A. Accompanying cartoon depicts protein localization patterns seen in early and mature (late) granular cells. **(G)** Optical sections through mature granular cells show prominent granules encased by thick keratin bundles. Single magenta channel reveals voids where KGs reside, indicative of caged KGs. Asterisks, statistically significant ($p < 0.05$). N.S., not significant.

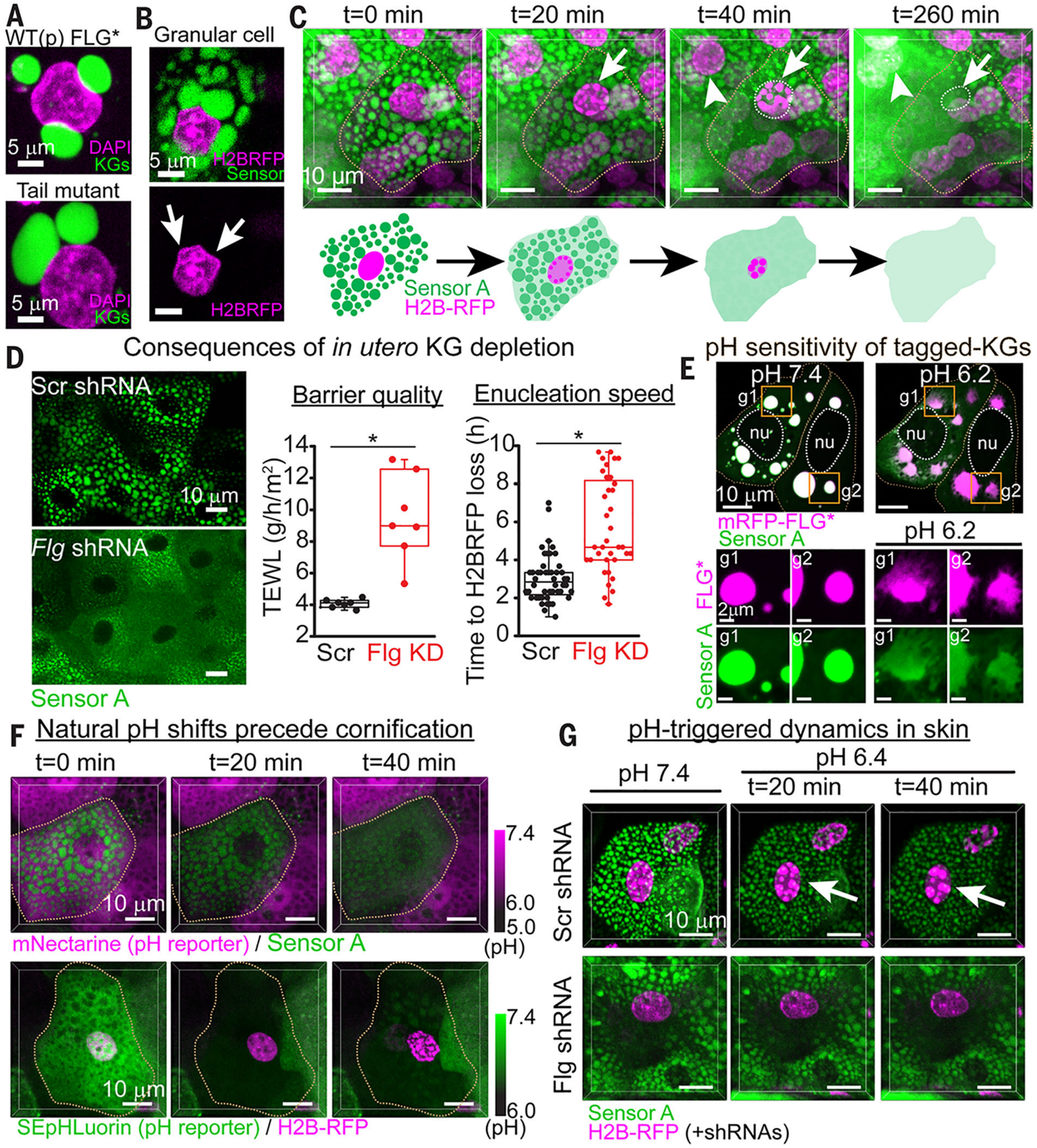

Fig. 7. Environmentally regulated KG dynamics drive skin barrier formation.

(A) Nucleus-KG interactions in HaCATs transfected with FLG variants. **(B)** Nucleus-KG interactions in a granular cell from live imaging of E18.5 mouse skin with resolution of nuclei (H2B-RFP) and KGs (sensor A). Arrows point to KG-associated nuclear deformations. **(C)** Granular cell–to–squame transition, as depicted by live imaging (3D view) of E18.5 mouse skin (movie S8). Early signs include chromatin compaction (arrows) and diminished partitioning of sensor within KGs. Late signs include KG disassembly and enucleation. **(D)** In utero Flg knockdown depletes KGs, causes a delay in enucleation, and partially compromises the skin barrier. Enucleation speeds were determined by live imaging of chromatin degradation. Barrier quality was measured as transepidermal water loss (TEWL). Asterisks, statistically significant ($p < 0.05$). **(E)** Effects of shifting the intracellular pH on KG dynamics of mRFP1-tagged FLG* and sensor A, as monitored by live imaging of HaCATs (maximum intensity projections). Note the rapid ($t = 5$ min) pH-triggered dissolution of KG components. g1 and g2 show individual granules. Sensor A mirrored the pH-triggered drop in the phase-separation capacity of FLG, which became increasingly cytoplasmic, reflected by a decrease in its partition coefficient ($P = 26$ at pH 7.4 to $P = 3.6$ at pH 6.2). nu, nucleus. **(F)** Live imaging (3D view) of enucleation and cornification in skin of embryos transduced to express an organelle marker (top: sensorA/KGs; bottom: H2BRFP/nuclei) and a pH reporter whose fluorescence is lost below pH 6.5. mNectarine (top) shows that when the intracellular pH of granular cells drops below pH 6.5, KGs begin to disassemble. SEpHLuorin reports a similar pH drop and shows that it precedes chromatin compaction. (G) Effects of pH-induced KG dynamics in sensor A^+ skin explants transduced with H2B-RFP and either Scr-shRNA (top) or Flg-shRNA (bottom). Note that chromatin compaction is not pH-triggered if KGs are missing altogether. See also figs. S19 to S24.